

SINGLET OXYGEN ENE REACTION: USING KINETIC ISOTOPE EFFECTS TO
PROBE TRANSIENT INTERMEDIATES

A Thesis

by

ANDREW KYLE JEFFRIES

Submitted to the Office of Graduate and Professional Studies of
Texas A&M University
in partial fulfillment of the requirements for the degree of

MASTER OF SCIENCE

Chair of Committee,	Daniel A. Singleton
Committee Members,	David E. Bergbreiter
	Frank M. Raushel
	Thomas D. Meek
Head of Department,	Simon W. North

August 2021

Major Subject: Chemistry

Copyright 2021 Andrew Jeffries

ABSTRACT

Pericyclic reactions generally occur through a single concerted transition state where all bonds are being formed and broken in a synchronous fashion. Previous experimental observations in the singlet oxygen ($^1\Delta_g$) ene reaction provide evidence to the contrary, suggesting that this particular pericyclic reaction occurs instead through two kinetically distinguishable steps. A more complete fundamental understanding of the enigmatic mechanism of this reaction is sought. In this work, intramolecular kinetic isotope effect studies of the $^1\text{O}_2$ ene reaction for simple, acyclic alkenes exhibit a weak temperature dependence. The low sensitivity of the product ratio on reaction temperature is interpreted as a diagnostic for a shallow peroxide intermediate that decays with a sub-picosecond half-life to form the hydroperoxide product.

However, this analysis assumes that the reaction obeys statistical rate theory. In the sub-picosecond time regime, intramolecular energy relaxation and intermediate decay can occur simultaneously, and the co-occurrence of these events can alter statistical product ratios predicted from transition state theory (TST). The experimental isotope effects measured here cannot be unambiguously reconciled with those predicted using statistical methods, which reinforces the suggestion that dynamic effects can influence the outcome of reactions that feature a formal intermediate.

ACKNOWLEDGEMENTS

First and foremost, I want to thank my mentor and friend Dr. Joe Workman. More than just being an incredible professor, you've helped me to achieve more than what I thought possible for myself, and I am sure you will inspire many others to do the same. Also, thanks to my graduate advisor Dr. Singleton. It was a joy to learn from you in class, group meetings, and impromptu office hours.

I am grateful for all the friends I have made in the past decade to laugh, smile, and share victories and struggles with. To Jessica, my special loved one, thank you for your love and compassion throughout my graduate education and beyond.

Lastly, I'd like to thank my mom and dad for their love and support. Thanks for cooking big breakfasts on standardized testing days, staying awake until the wee hours of the morning to help me finish last-minute school projects, and helping me believe that I can do anything I set my mind to.

CONTRIBUTORS AND FUNDING SOURCES

Contributors

This work was supervised by a thesis committee consisting of Dr. Daniel Singleton (advisor), Dr. David Bergbreiter and Dr. Frank Raushel from the Department of Chemistry, and Dr. Thomas Meek from the Department of Biochemistry and Biophysics. All other work conducted for the thesis was completed by the student independently.

Funding Sources

This graduate study was supported in part by the Texas A&M Department of Chemistry Teaching program. The work was also supported by the National Institute of Health (NIH) Grant GM-45617.

TABLE OF CONTENTS

	Page
ABSTRACT.....	ii
ACKNOWLEDGEMENTS.....	iii
CONTRIBUTORS AND FUNDING SOURCES	iv
TABLE OF CONTENTS.....	v
LIST OF FIGURES	vii
LIST OF TABLES.....	ix
CHAPTER I INTRODUCTION.....	1
General Overview	1
Kinetic Isotope Effects.....	3
Bifurcating Energy Surfaces.....	5
CHAPTER II INTRAMOLECULAR ISOTOPE EFFECTS IN THE SINGLET OXYGEN ENE REACTION.....	12
Previous Work	12
Experimental Results and Discussion.....	19
Computational Studies.....	22
Statistical Models.....	24
Trajectory Studies	30
CHAPTER III EXPERIMENTAL PROCEDURES.....	37
Synthesis Details.....	37
Synthesis of tetramethylethylene- <i>trans</i> -d ⁶	37
Synthesis of tetramethylethylene-gem-d ⁶	41
Synthesis of (Z)-3,4-dimethyl-3-hexene-d ³	43
Synthesis of (Z)-7,8-dimethyl-7-tetradecene.....	48
(Z)-7,8-dimethyl-7-tetradecene ¹ O ₂ Ene Reaction Kinetics	53
¹ O ₂ Ene Reaction KIE Procedure.....	55
KIE Measurement Procedure.....	56
VNMRJ Macro.....	57
KIE Formulae and Raw Integrations	59
Calculational Procedures	67

CHAPTER IV CONCLUSION	71
REFERENCES	72
APPENDIX.....	77

LIST OF FIGURES

	Page
Figure 1. a) A reaction coordinate diagram depicting a bimolecular reaction occurring in a single step. Rate constant can be calculated from Equation 1. b) Another reaction coordinate diagram with two reaction channels through which A and B can react. Kinetic product selectivity can be calculated from Equation 2.	2
Figure 2. Inclusion of zero-point energy (ZPE) on reaction coordinate diagrams as an aid for visualizing kinetic isotope effects. a) KIE for the E2-type elimination of 1-bromobutane. b) H/D KIE for the E1-type elimination of 2-bromo-2-methylpentane.	3
Figure 3. a) Example of a symmetrical bifurcating surface containing two adjacent transition states without an intervening intermediate. b) An unsymmetrical bifurcating surface showing the MEP connected to only one of the two products. c) A PES featuring a shallow intermediate with two symmetric exit channels toward products.	6
Figure 4. a) Dimerization of cyclopentadiene, which exhibits two adjacent bispericyclic (TS1) and Cope rearrangement (TS2) transition states on a symmetrical bifurcating PES. b) A Diels-Alder reaction that affords a mixture of the two possible cycloadducts via an asymmetric bifurcating PES. c) An intramolecular rhodium-carbenoid C-H insertion reaction that operates on an asymmetric bifurcating PES.	9
Figure 5. Proposed mechanisms for the $^1\text{O}_2$ ene reaction.	13
Figure 6. Inter- and intramolecular ^{13}C and H/D kinetic isotope effects for the reaction of tetramethylethylene with $^1\text{O}_2$	14
Figure 7. a) Product distribution of the reaction of $^1\text{O}_2$ with 2-deuteriomethyl-2-pentene resulting from two diastereotopic rate-determining transition states, illustrating the cis effect. b) Reaction of top-face and bottom-face peroxides of deuterium-labelled 2-methyl-2-pentene showing the stereospecificity of proton/deuterium abstraction from the ethyl group.	16
Figure 8. Qualitative reaction coordinate diagram for reaction of 5 with $^1\text{O}_2$	21
Figure 9. Intrinsic reaction coordinate (IRC) diagrams for the conversion of peroxide to hydroperoxide using several DFT methods.	24
Figure 10. VTST isotope effect predictions and the effect of temperature on the isotopic partitioning.	25

- Figure 11. Top: A generalized structure for the proton abstraction transition state from the perepoxide intermediate. The developing C-O bond is labelled as r_{C-O} , and a dashed line connects the proton to be abstracted to the terminal oxygen. Bottom: A plot of r_{C-O} versus the QUIVER-predicted intramolecular ^{13}C KIE, with the experimental value for the olefinic carbon shown above. Each data point gives a KIE prediction using a unique DFT method, and the legend is used to describe the potential energy barrier height of the product-determining transition state. 27
- Figure 12. Top: A representative structure for the 1O_2 /TME system showing the two chosen internal coordinates. Bottom: A potential energy contour plot of the 1O_2 /TME system with the two C(alkene)-O bond distances plotted in the xy plane and potential energy plotted as contour lines. 31
- Figure 13. Equations used to calculate the intramolecular kinetic isotope effects for both tetramethylethylene-*trans*- d^6 (7), tetramethylethylene-*gem*- d^6 (11), and 3,4-dimethylhexene- d^3 (18). The raw integrations used for each product are highlighted in the structure of each isotopomer. 59
- Figure 14. 1H NMR spectrum of 1O_2 reaction with tetramethylethylene at 55% conversion after application of VNMRJ macro. 60
- Figure 15. Bottom: Expansion of aliphatic 1H NMR peaks belonging to tetramethylethylene and allylic alcohol product. Top: Expansion of olefinic peaks between 5.2 and 4.4 ppm. 61
- Figure 16. Example 1H NMR spectrum of 1O_2 ene reaction of 3,4-dimethylhexene- d^3 . All species represented in the spectrum are displayed above. Top: Expansion of olefinic 1H NMR peaks belonging to major and minor regioisomeric allylic alcohols and starting material contaminant. Bottom: Expansion of aliphatic peaks. 62
- Figure 17. 1H NMR of mixture of regioisomeric mixture of alcohols resulting from the 1O_2 ene reaction of (*Z*)-7,8-dimethyl-7-tetradecene. H_d and H_e overlap with the methylene protons in the aliphatic chain, rendering quantitation difficult. 63
- Figure 18. Potential energy profiles connecting starting materials to intermediate for several DFT method/basis set combinations. 69

LIST OF TABLES

	Page
Table 1. Intramolecular H/D KIEs for the ene reaction of singlet oxygen with deuterium-labelled alkenes measured by quantitative ^1H NMR. Experimental uncertainties are given as 95% confidence intervals and are based on six measurements at each indicated temperature. Reactions were conducted in acetone- d^6 on a 100 μmol scale in an NMR tube.....	19
Table 2. Results of trajectory simulations and CVT/SCT predictions of the intramolecular isotope effects of 5 and 6 at -96°C and 25°C	33
Table 3. Raw integrations and calculated kinetic isotope effects for the singlet oxygen ene reaction of tetramethylethylene- <i>trans</i> - d^6	64
Table 4. Raw integrations and calculated kinetic isotope effects for the singlet oxygen ene reaction of tetramethylethylene- <i>gem</i> - d^6	65
Table 5. Raw integrations and calculated kinetic isotope effects for the singlet oxygen ene reaction of 3,4-dimethylhexene- d^3	66
Table 6. DFT methods used to model the decomposition of the perepoxide intermediate and their corresponding barrier heights, developing C-O bond lengths, and intramolecular olefinic ^{13}C KIEs. The methods highlighted in red were used to calculate the IRCs and VTST KIEs in Figures 8 and 9.....	67

CHAPTER I

INTRODUCTION

General Overview

An important fundamental problem in modern organic chemistry is the understanding of reaction mechanisms. If the correct mechanism for a reaction has been established, then experimental outcomes such as stereo- and regiochemistry of product formation or amount of time required for reaction completion can be controlled by changing the reaction conditions in a rational way. These goals are useful both from a practical and theoretical perspective, as new synthetic methods are developed by better understanding old ones. Transition state theory is the primary theoretical tool organic chemists use to interpret mechanistic experiments. Organic chemists have developed the ability to conceptualize a chemical reaction in terms of a reaction coordinate diagram, and transition state theory provides a connection between reaction coordinate diagrams and reaction rate.

Consider a bimolecular reaction between hypothetical starting materials A and B that react in a single step to form a single product C (Figure 1a). If the relative free energies of the starting materials and the transition state (AB^\ddagger) that connects them to the product are known, then the second order rate constant for the conversion of starting materials to products can be calculated at any temperature. This relationship is expressed

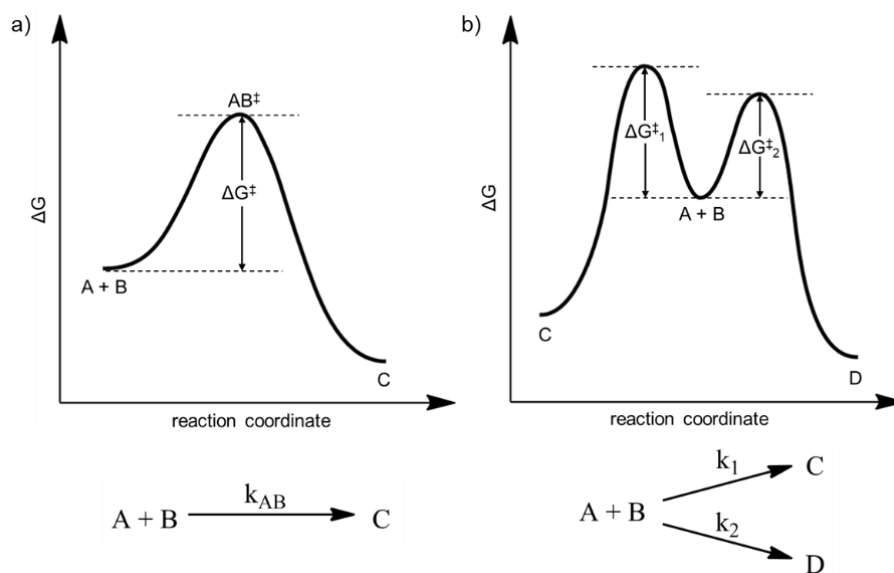


Figure 1. a) A reaction coordinate diagram depicting a bimolecular reaction occurring in a single step. Rate constant can be calculated from Equation 1. b) Another reaction coordinate diagram with two reaction channels through which A and B can react. Kinetic product selectivity can be calculated from Equation 2.

mathematically in the Eyring equation (Equation 1), which allows a prediction of the rate constant of a reaction from the free energy of activation (ΔG^\ddagger) and temperature.

If instead, two competing reaction channels passing over two separate transition states to give two products (C and D) are considered (Figure 1b), then product selectivity can be calculated directly from the ratio of the rate constants. This statement is only valid if the reaction is under kinetic control, that is, if the relative amount of C and D at any time during the reaction is decided only by their relative rates of formation and not their relative free energy content. When this is the case, then the simplest way to control the product ratio would be to change the reaction temperature, since there is an inverse exponential dependence of the rate ratio on temperature (Equation 2). This temperature dependence can

be observed in a surprising number of phenomena in organic chemistry, including regio- and stereoselectivity.

$$k_{AB} = \kappa \frac{k_b T}{h} e^{-\Delta G^\ddagger / RT} \quad (\text{Eqn. 1})$$

$$\frac{k_1}{k_2} = e^{-(\Delta G_1^\ddagger - \Delta G_2^\ddagger) / RT} \quad (\text{Eqn. 2})$$

Kinetic Isotope Effects

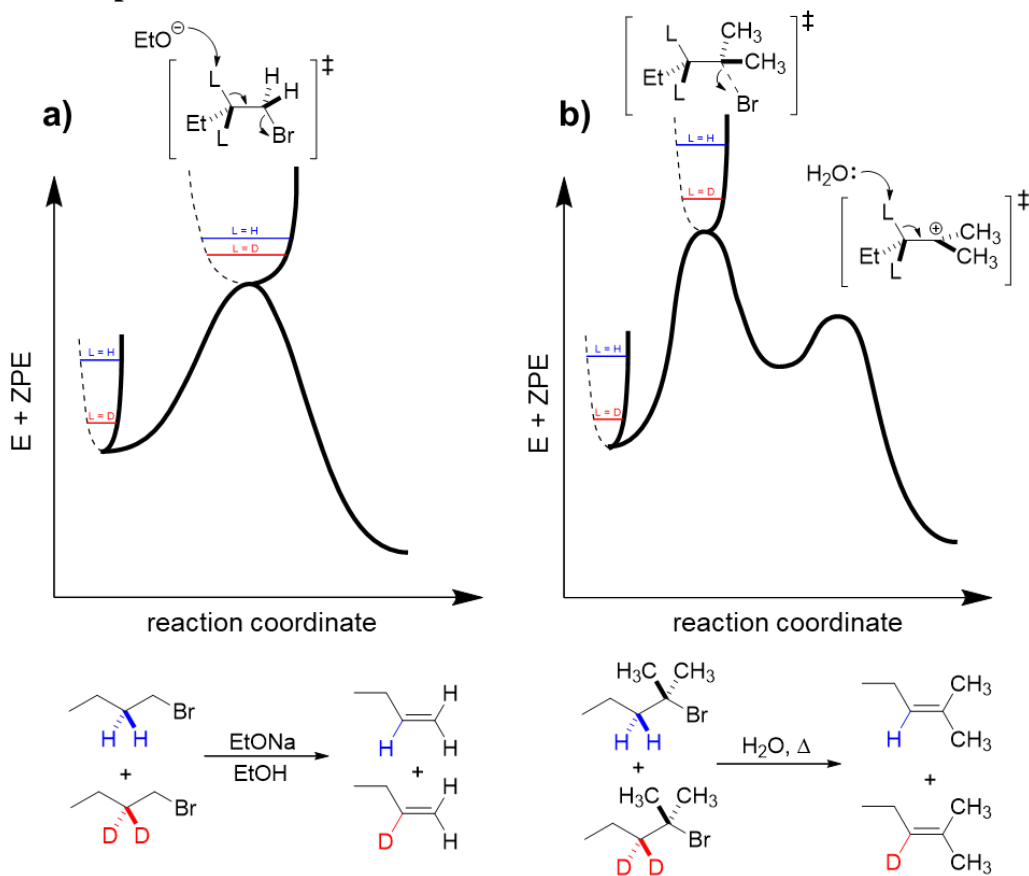


Figure 2. Inclusion of zero-point energy (ZPE) on reaction coordinate diagrams as an aid for visualizing kinetic isotope effects. a) KIE for the E2-type elimination of 1-bromobutane. b) H/D KIE for the E1-type elimination of 2-bromo-2-methylpentane.

Kinetic isotope effects are influenced by temperature in the same way. Measurement of intermolecular kinetic isotope effects (KIEs) is a method used to probe the rate-limiting step of a reaction. Intermolecular KIEs report on which atoms are involved in the rate-limiting step by measuring the ratio of the rates between “light” and “heavy” isotopes of an atom in a reacting species. The isotopic labelling introduces a small difference in the activation energies for the two isotopomers, which in turn causes a temperature dependence on the selection between the products.

As an illustrative example, intermolecular isotope effects have been measured for elimination reactions of alkyl halides (Figure 2). In order to measure the isotope effects, a 1:1 mixture of the labelled and unlabeled alkyl halides is subjected to reaction conditions designed to encourage E2- or E1-type elimination. The ratio of isotopomeric products is determined using quantitative techniques - most commonly ^1H NMR. The isotopomers will react at slightly different rates, which is reflected in the product ratio if the reaction is under kinetic control. This difference in activation energies can be approximated as the zero-point energy (ZPE) difference from starting materials to products (Equation 3).

$$\frac{k_H}{k_D} \approx e^{-(\Delta\text{ZPE}_H^\ddagger - \Delta\text{ZPE}_D^\ddagger)/RT} \quad (\text{Eqn. 3})$$

Isotopic perturbation to a heavier isotope translates to a decrease in ZPE for all vibrational modes that involve motion of the perturbed atom. Because $\Delta\text{ZPE}_H^\ddagger$ is lower than $\Delta\text{ZPE}_D^\ddagger$ for both reactions, the rate ratio calculated using Equation 3 will be greater than unity, which results in a normal KIE.

The magnitude of the isotope effects allows a qualitative interpretation of the mechanism of each reaction. A large primary ($k_H/k_D = 2.0 - 7.0$) KIE of 6.7 observed in the formation of 1-butene from 1-bromobutane implicates the involvement of C-H bond breaking in the rate-limiting transition state of the reaction, which is consistent with an E2 mechanism. A smaller secondary ($k_H/k_D = 1.0 - 1.4$) KIE for the E1-type elimination reaction of 2-bromo-2-methylpentane indicates that the C-H bond is not breaking in the rate-limiting transition state. The small rate increase for the perproteo relative to the deuterated alkyl halide in this case is due to the stabilization of the incipient carbocation via hyperconjugation.

Using modern computational methods, KIEs can be predicted to give molecular-level detail about transition states in the mechanism. Given the molecular geometry at the transition state, the KIE can be predicted from the calculated vibrational frequencies using the Bigeleisen method.¹ Comparison of KIEs predicted in this way to those acquired from experiment can give accurate bond-breaking and bond-forming distances, which is akin to a “transition state spectroscopy”.² This technique is inherently limited since it measures the vibrational frequencies from the same position on the potential energy surface regardless of the contribution of temperature and entropy to the “true” location of the TS. Variational transition state theory (VTST) differs from this approach because it minimizes the rate constant with respect to the reaction coordinate at any given temperature.³

Bifurcating Energy Surfaces

Although selectivity can be determined from *separate* transition states in this way, the same cannot be done for two products originating from the *same* transition state. It is not immediately clear how a single transition state could connect to more than one intermediate or product if the reaction coordinate is conceived in the traditional two-dimensional sense. A complete description of how the potential energy of a reaction changes with molecular geometry requires $3N - 6$ geometric coordinates for nonlinear systems.⁴ If two of these $3N - 6$ coordinates are suitably chosen and added to the two-dimensional reaction coordinate, then the 2D energy profile becomes a cross-sectional “slice” of the new 3D representation of the potential energy surface (PES). With this new perspective, it is easier to visualize how a transition state can bifurcate into two different products, and perhaps more interestingly, how two transition states could be adjacent in a

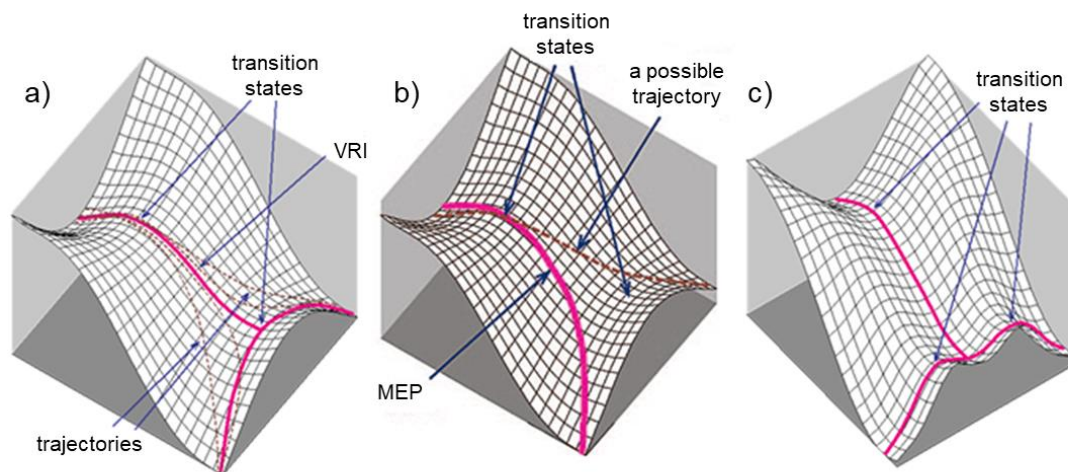


Figure 3. a) Example of a symmetrical bifurcating surface containing two adjacent transition states without an intervening intermediate. b) An unsymmetrical bifurcating surface showing the MEP connected to only one of the two products. c) A PES featuring a shallow intermediate with two symmetric exit channels toward products.

reaction coordinate without an intervening intermediate. The absence of an intermediate on such a PES gives rise to a two-step no-intermediate mechanism (Figure 3a).

The minimum energy path (MEP) on the bifurcating surface in Figure 3a occurs in two stages: the first stage traces a line directly downhill from TS1 towards TS2, and a valley-ridge inflection (VRI) occurs between TS1 and TS2 when the second derivative of the potential energy with respect to the orthogonal coordinate becomes zero. This means that the landscape of the surface changes from a valley to a ridge at this point, and the path begins to curve upwards although it is still decreasing in energy towards TS2. The second stage is split into two directions orthogonal to the first stage and leads to two separate products. The point at which these two paths intersect is a formal saddle point (TS2) that connects the two product minima. This is a prototype for a symmetric bifurcating energy surface, in which the rate-limiting transition state (TS1) contains a symmetry element (e.g. C_s or C_2) that, upon its operation, interconverts the two degenerate intermediates or products.⁵

There are two variations of the symmetrical bifurcating PES that can describe chemical systems – asymmetric bifurcating surfaces (Figure 3b) and surfaces containing a shallow intermediate well (Figure 3c). The selectivity on these types of surfaces can only be predicted by considering the detailed motions and momenta of the atoms, or dynamic trajectories, as the system descends from the rate-limiting transition state. On an asymmetric bifurcating PES, the MEP only connects to one of the possible products. The alternative product is accessible via TS2, which interconverts the two product minima. TST

fails to predict selectivity in these cases because the rate-limiting TS1 connects to only one product, while dynamic trajectories have shown that both products can be formed from TS1. Instead of the first stage of the MEP descending directly to another transition state (TS2), it could encounter a shallow minimum (Figure 3c). Two symmetry-related saddle points connect this common intermediate to two separate products. Product selectivity could be predicted in these cases by TST, but it is often the case that these predictions are inconsistent with experimental selectivities for surfaces of this type. If this intermediate is sufficiently shallow, then it can evade direct experimental detection using all but the most sensitive techniques due to its short lifetime.⁶

In short, a bifurcating PES occurs when a single transition state allows a choice between two intermediates or products without subsequent barriers to their formation. It is a useful theoretical construct with many practical applications to common organic reactions, and many still yet to be realized.⁷ Bifurcating surfaces have been studied by several research groups over the past few decades with the goal of determining the factors that are most important in dictating product selectivity. Some examples of reactions with bifurcating potential energy surfaces are shown in Figure 4.

The most ubiquitous application of bifurcating energy surfaces to chemical systems is to pericyclic reactions.⁸ The prototypical example in the literature is the dimerization of cyclopentadiene, in which the [2+4] and [4+2] transition states have merged into a single “bispericyclic” TS that connects to the two degenerate cycloadducts (Figure 4a).⁹ The

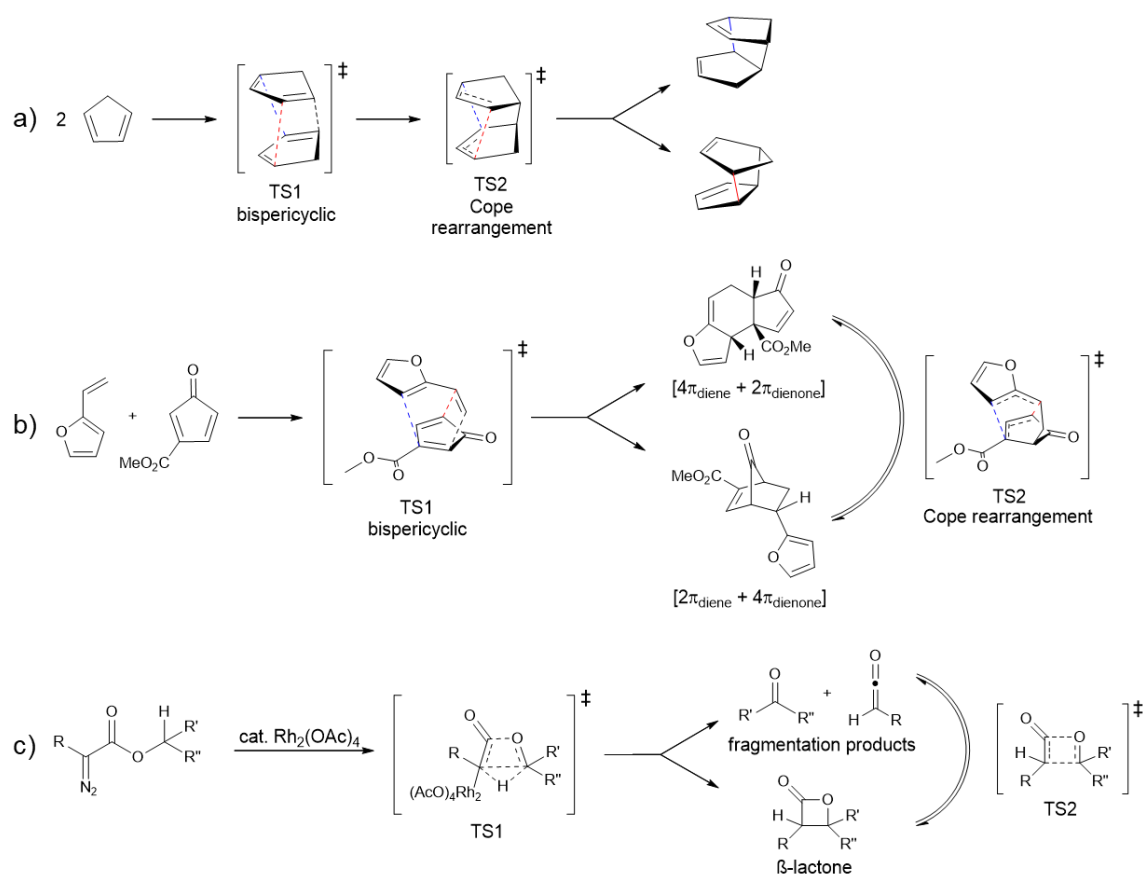


Figure 4. a) Dimerization of cyclopentadiene, which exhibits two adjacent bispericyclic (TS1) and Cope rearrangement (TS2) transition states on a symmetrical bifurcating PES. b) A Diels-Alder reaction that affords a mixture of the two possible cycloadducts via an asymmetric bifurcating PES. c) An intramolecular rhodium-carbenoid C-H insertion reaction that operates on an asymmetric bifurcating PES.

periselectivity is decided on a symmetrical bifurcating energy surface, and the selectivity of a reaction operating on a symmetric bifurcating surface is intuitively 1:1.

While the 1:1 periselectivity for the dimerization of cyclopentadiene is trivial due to the symmetry of the PES, there is no straightforward prescription for predicting selectivity on unsymmetrical bifurcating surfaces. Asymmetry is introduced when the addends are nonequivalent, as in the case of the Diels-Alder cycloaddition of 2-vinylfuran

and 3-methoxycarbonylcyclopentadienone (Figure 4b). This choice of reactants strikes an electronic balance between the two addends so that either could act as the diene or dienophile in the reaction. Experiments show that a 1.6:1 ratio of $[2\pi_{\text{diene}} + 4\pi_{\text{dienone}}]$ and $[4\pi_{\text{diene}} + 2\pi_{\text{dienone}}]$ endo cycloadducts was afforded as the kinetic mixture.¹⁰ However, the MEP only leads to the majority $[2\pi_{\text{diene}} + 4\pi_{\text{dienone}}]$ product. Surprisingly, two distinct transition states leading to $[4\pi_{\text{diene}} + 2\pi_{\text{dienone}}]$ and $[2\pi_{\text{diene}} + 4\pi_{\text{dienone}}]$ do not control the product distribution in this reaction! Equation 2 cannot be used to predict the product ratio because there are not two separate barriers governing the rate of formation of each product. Unsymmetrical bifurcating surfaces have more practical applications for organic chemists because they can describe systems that give two nonequivalent products from a single TS. Factors that control the product ratio in these cases are only qualitatively understood, and only dynamic trajectory studies have succeeded in correctly predicting a mixture of products.

Applications of bifurcating surfaces have begun to expand to more diverse systems, including carbocation rearrangements,¹¹ nucleophilic substitution reactions,¹² and transition metal catalyzed reactions.¹³ A rhodium-catalyzed intramolecular C-H activation reaction was recently reported to exhibit reactivity that is consistent with an unsymmetrical bifurcating energy surface.¹⁴ In the reaction, a Rh-carbenoid proceeds through a single ambimodal TS to either a β -lactone or to two separate ketone and ketene fragments (Figure 4c). If fragmentation arises as the result of a PES bifurcation, then changing the reaction temperature to favor the β -lactone will not be effective since the rates of formation of the

β -lactone and fragmented products are decided by the same barrier. Eliminating unwanted side products by changing reaction conditions is highly sought after in organic synthesis, so a deeper understanding of the factors that decide selectivity on asymmetric bifurcating surfaces is necessary.

For reactions operating on a PES containing a shallow intermediate, TST can provide a prediction of selectivity because there are two separate transition states leading from the intermediate well to the two separate products. If both product-determining barriers are the same height, then the selectivity of the reaction would be 1:1, as in the case of a symmetric bifurcating PES. The nature of the selectivity becomes less trivial when the PES with a shallow intermediate is desymmetrized, which could be accomplished by introducing an isotopic perturbation. Selectivity predictions on surfaces of this type is complicated because it is possible for dynamic trajectories to bypass shallow minima, and these trajectories cannot be accounted for using simple statistical models.¹⁵ Existing statistical models mispredict the outcome of reactions that operate on these types of potential energy surfaces in subtle ways that using dynamics simulations can rectify.

CHAPTER II
INTRAMOLECULAR ISOTOPE EFFECTS IN THE SINGLET OXYGEN ENE
REACTION

Previous Work

Triplet molecular oxygen, because of the stability imparted to it by its exceptional ground state electronic structure, has high kinetic barriers to reaction with most common organic functional groups.¹⁶ The discovery of a method for the *in situ* generation of singlet ($^1\Delta_g$) oxygen in the solution phase triggered the exploration of its utility as a reactive intermediate to enable previously inaccessible chemistry.¹⁷ Singlet oxygen has several possible reaction channels through which it can react with alkenes, including [4 + 2] cycloadditions with dienes, [2 + 2] cycloadditions with electron-rich alkenes such as enol ethers, and the ene reaction to afford allylic hydroperoxides. The latter reaction mode and the peculiar nature of its mechanism has been debated extensively for the past half-century, and the identity of the intermediate, if one exists, is still a question without a satisfying answer.

Some mechanistic possibilities for a prototypical $^1\text{O}_2$ ene reaction are shown in Figure 5. A concerted mechanism would involve a chairlike transition state postulated in typical sigmatropic rearrangements, but the intermediacy of perepoxides, zwitterions/diradicals, and exciplexes have also been supported in the literature. Recently, a computational study of this reaction supported a mechanism which lacks an intermediate, yet still proceeds through two kinetically distinguishable steps.¹⁸ It will be the goal of this

research to test the validity of this “two-step no-intermediate” mechanism and to explore possible alternatives to the current understanding of this enigmatic mechanism of $^1\text{O}_2$ with alkenes.

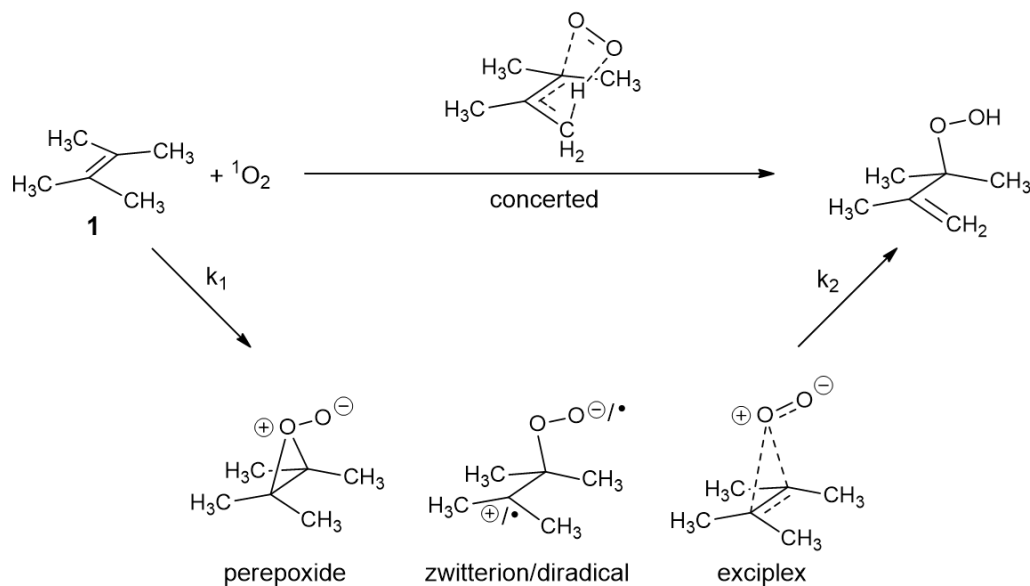


Figure 5. Proposed mechanisms for the $^1\text{O}_2$ ene reaction.

The reaction under study has a rich history of experimental work aimed at elucidating fine details of the mechanism and how it can change depending on the substitution pattern of the alkene. Previous investigation of the kinetics of the $^1\text{O}_2$ ene reaction of various di-, tri-, and tetrasubstituted alkenes indicated that formation of the activated complex is entropy controlled and that there is little variation in the magnitude of the second-order rate constant with the nature of the solvent.¹⁹ The rate constants vary by less than an order of magnitude from CS_2 to acetone- d^6 , which is inconsistent with a rate-limiting transition state with considerable charge separation. It should be noted that these

Eyring parameters are influenced only by mechanistic steps up to and including the rate-limiting step.

A common method of studying the rate-limiting step in a reaction is to measure a kinetic isotope effect, which is a measure of the relative rates of isotopically labelled materials compared to their unlabeled counterparts. As shown in Figure 6, intermolecular ^2H and ^{13}C KIEs have been measured previously for the reaction of $^1\text{O}_2$ with unlabelled and d^{12} -tetramethylethylene (TME) (**1** versus **2**) and a slightly modified variant of TME (**3**).^{18a, 20} A qualitative evaluation of the intermolecular ^{13}C KIEs suggests that there is an

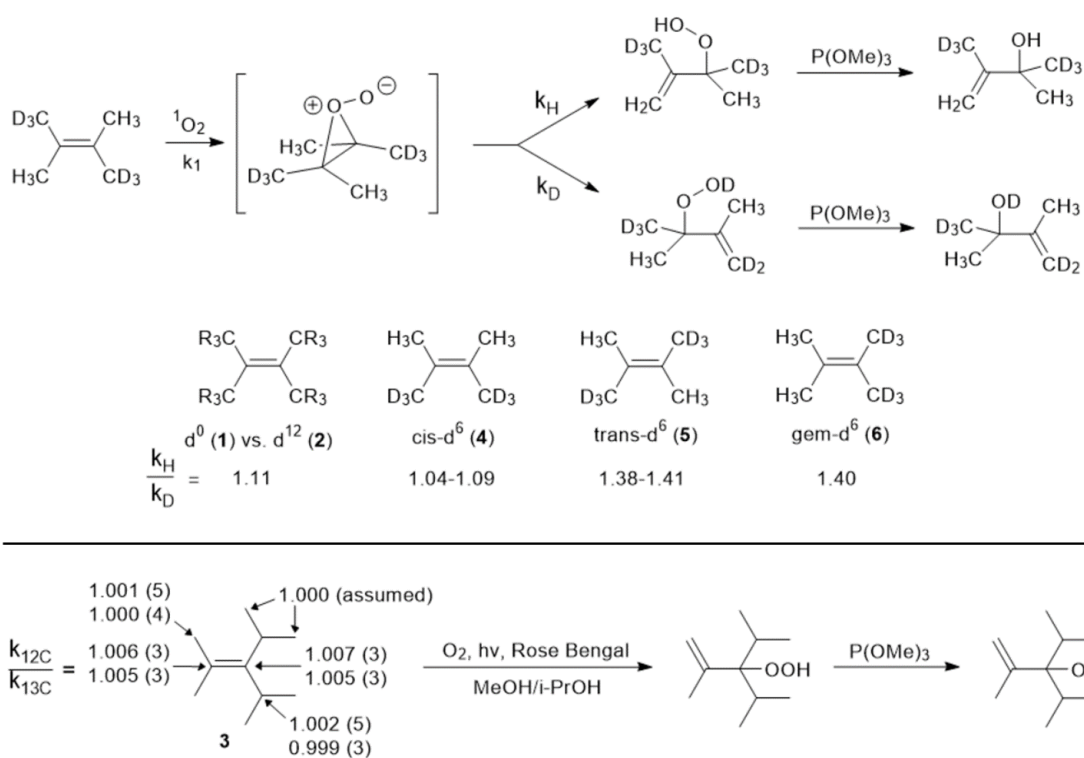


Figure 6. Inter- and intramolecular ^{13}C and H/D kinetic isotope effects for the reaction of tetramethylethylene with $^1\text{O}_2$.

equal extent of C-O bond formation to both alkene carbons at the rate-limiting transition state because of the primary ^{13}C isotope effects observed on both olefinic carbons of **3**. There is little to no allylic C-H bond involvement in the rate-limiting transition state indicated by the negligible intermolecular ^2H KIE.

Intramolecular KIEs provide information on competition between stereochemically distinct sites in a molecule. This isotopic competition is available to compounds **5** and **6**, but not for **4**, resulting in a smaller intramolecular ^2H KIE for **4**. This experiment, known as the “Stephenson isotope effect test”, can not only discern stepwise from concerted mechanisms in pericyclic reactions but it also gives information on the symmetry of the intermediate species.²¹ The observation of intermolecular KIEs that differ from intramolecular KIEs is the basis of an argument for a stepwise mechanism.²² An intermediate perepoxide has therefore been supported since an intermediate with the symmetry of a perepoxide is able to discriminate between methyl and deuteriomethyl groups on the same side of the alkene. A concerted mechanism has been ruled out because of the observation of two kinetically distinguishable steps. This type of behavior has also been observed in allene dimerizations where isotopic discrimination occurs during a barrierred product-determining step that is separate from the rate-determining step.²²⁻²³

Other experimental studies on the $^1\text{O}_2$ ene reaction of trisubstituted alkenes have shown that there is a regiochemical preference for proton abstraction from the more substituted side of the alkene.²⁴ This general type of selectivity has been named the ‘cis effect’ in the chemical literature. This observed regiochemistry is consistent with the

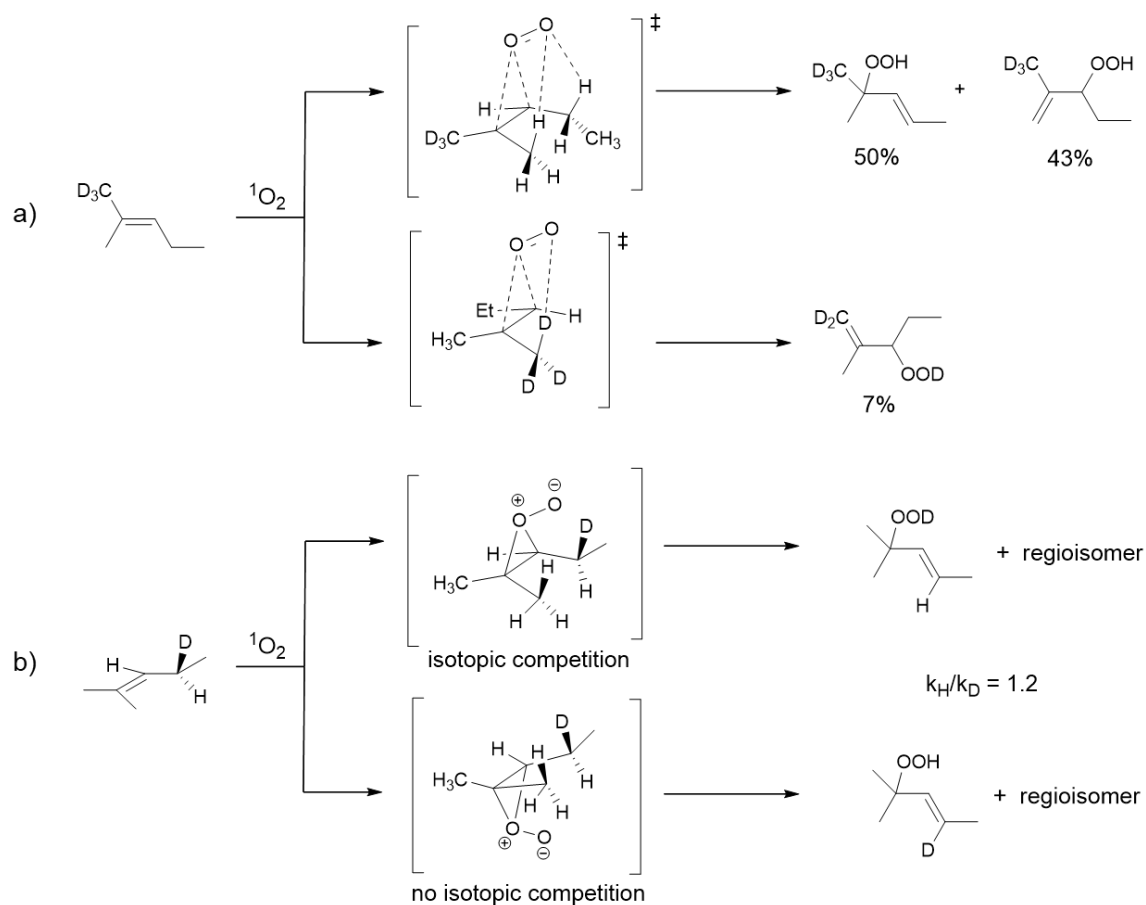


Figure 7. a) Product distribution of the reaction of $^1\text{O}_2$ with 2-deuteriomethyl-2-pentene resulting from two diastereotopic rate-determining transition states, illustrating the cis effect. b) Reaction of top-face and bottom-face peroxides of deuterium-labelled 2-methyl-2-pentene showing the stereospecificity of proton/deuterium abstraction from the ethyl group.

existence of two competitive rate-limiting transition states leading to two diastereomeric peroxides, as seen in the $^1\text{O}_2$ ene reaction of 2-trideuteriomethyl-2-pentene (Figure 7a). Allylic hydrogen bonding type interactions in these transition states have been proposed to result from the interaction of an empty π^* orbital from the approaching $^1\text{O}_2$ with filled allylic C-H σ orbitals.²⁵ The nearly equal amount of secondary versus tertiary

hydroperoxide products indicates that there are no Markovnikov-type directing effects in the reaction from the formation of a carbocation or radical at the tertiary versus secondary center and provides evidence against an open biradical or zwitterionic intermediate.

Many more subtle regiochemical effects have been explored,²⁶ but experimental results of the reaction of $^1\text{O}_2$ with simple alkenes all reinforce the idea that proton abstraction is preferred on the more substituted side of alkenes due to “hydrogen bonding” with a greater amount of alkyl substituents. This interaction could explain the small intermolecular isotope effect observed in the reaction of d^0 - versus d^{12} -labelled TME. An alternative explanation of this effect claims that the lower rotational barriers of cis-alkyl substituents provides a higher reactivity than trans-alkyl substituents, but this reasoning has not held up to further scrutiny.²⁵

Solvent effects on the product selectivity and the rate of the reaction of unlabelled 2-methyl-2-pentene with $^1\text{O}_2$ have also been studied. It was determined that both the ratio of rate constants for singlet oxygen decay versus reaction with 2-methyl-2-pentene and the ratio of secondary to tertiary hydroperoxide formed are independent of the dielectric constant of the solvent used in the reaction. Generally, $^1\text{O}_2$ ene reactions show little variation in rate and selectivity with changes in solvent polarity, which is consistent with low enthalpies of activation for rate-determining and product-determining steps. Because of the low enthalpy of activation for the bimolecular association of $^1\text{O}_2$ and alkene and conversion of the perepoxide to the hydroperoxide in the reaction, solvent effects generally only change product-determining and rate-determining barriers by less than an order of

magnitude for $^1\text{O}_2$ ene reactions even though there is a significant amount of charge buildup and dissipation for the formation and decomposition of the perepoxide respectively.

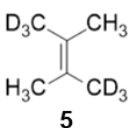
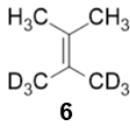
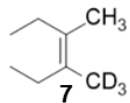
The stereochemical outcome of the reaction has been investigated in the reaction of a stereospecifically labelled 2-methyl-2-pentene isotopomer as shown in Figure 7b. The reaction gives exclusively (E)-alkene when a proton or deuterium is abstracted from the ethyl group. Formation of the (Z)-alkene is discouraged by the developing $A^{1,3}$ strain in the transition state for inward rotation of the ethyl group. The $A^{1,3}$ strain locks the ethyl group into a preferred conformation that presents a proton to one face of the alkene and a deuterium to the opposite face. The measured H/D isotope effect of 1.2 is an average of the KIEs observed for isotopic competition on the same side of the alkene on one face and no isotopic competition on the opposite face. This outcome confirms that the $^1\text{O}_2$ ene reaction occurs via a nominally suprafacial process such that when the intermediate is formed, rotation of the central C-C bond does not occur. This again provides evidence against an open intermediate (biradical or zwitterion) and reinforces a perepoxide.

Despite the evidence for a stepwise mechanism, it is not clear if the reaction proceeds through an intermediate species. Such an intermediate has been indirectly detected in the case of the perepoxide generated from *trans*-cyclooctene, which lives on a time scale that is sufficiently long for intermolecular trapping with triphenyl phosphite.²⁷ However, attempted trapping of an intermediate using cyclopropyl-substituted olefins as mechanistic probes in simple, acyclic systems has been unsuccessful.²⁸ This study proves that the intermediate perepoxide, if it exists, has a very short lifetime, since the first order

rate constant for cyclopropyl radical ring opening is $\sim 10^9 \text{ s}^{-1}$.²⁹ Therefore, any additional experimental support for the existence of a perepoxide from **1** will have to be gained indirectly.

Experimental Results and Discussion

Table 1. Intramolecular H/D KIEs for the ene reaction of singlet oxygen with deuterium-labelled alkenes measured by quantitative ^1H NMR. Experimental uncertainties are given as 95% confidence intervals and are based on six measurements at each indicated temperature. Reactions were conducted in acetone- d^6 on a 100 μmol scale in an NMR tube.

olefin	temperature ($^{\circ}\text{C}$)	$k_{\text{H}}/k_{\text{D}}$	TST	UM06/6-31+G** CVT/SCT
 5	-96	1.38 ± 0.01	1.64	1.18
	-78	1.38 ± 0.01	1.57	1.17
	21	1.35 ± 0.01	1.35	1.16
	56	1.35 ± 0.01	1.31	1.16
 6	-96	1.57 ± 0.01	1.88	1.56
	-78	1.55 ± 0.01	1.77	1.54
	21	1.47 ± 0.01	1.47	1.46
	56	1.45 ± 0.01	1.40	1.44
 7	-78	1.55 ± 0.01	1.72	1.76
	21	1.44 ± 0.01	1.44	1.62
	56	1.44 ± 0.01	1.38	1.59

Towards this end, the temperature dependence of the intramolecular KIEs for a series of deuterium-labelled alkenes has been studied, and the results are displayed in Table 1. All alkenes were synthesized according to established literature procedures with minor modifications.³⁰ Dye photosensitization with Rose Bengal was employed to generate $^1\text{O}_2$. $\text{P}(\text{OMe})_3$ was added at the beginning of each reaction to prevent accumulation of the hydroperoxide, which was found to oxidize the photosensitizer in acetone- d^6 at elevated

temperatures. To determine if the presence of P(OMe)₃ affects the intramolecular isotopic selection, **6** was subjected to the reaction conditions without P(OMe)₃ in acetone-d⁶ at -78°C, at which minimal side-product formation was observed. The values with and without P(OMe)₃ are indistinguishable from one another, indicating the lack of a medium effect on the selectivity. Small temperature dependences such as those observed here are difficult to detect unless care has been taken to eliminate impurities from the labelled alkene and ensure that the quantitative ¹H NMR methodology is sufficient to measure relative amounts of ¹H nuclei with an accuracy of ±1%.³¹

A proposed qualitative energy diagram that accounts for the intramolecular isotope effects measured above is shown in Figure 8. In the reaction coordinate diagram, a shallow perepoxide intermediate is flanked on either side by a rate determining (TS1) and a product determining (TS2) transition state. TS1 decides which side of the alkene the proton is abstracted from, while TS2 determines the preference between alkyl groups on the same side of the alkene. Even with this information, it is difficult to change the reaction conditions to favor the formation of a single regioisomer in this reaction. As mentioned previously, a product-determining selection between methyl and deuteriomethyl groups on the same side of the alkene from a perepoxide intermediate could explain the observed isotope effects. The higher isotope effects measured for **6** compared to **5** is consistent with the idea that a proteomethyl group is better at stabilizing an incipient carbocation in the product-determining transition state than a deuteriomethyl group.

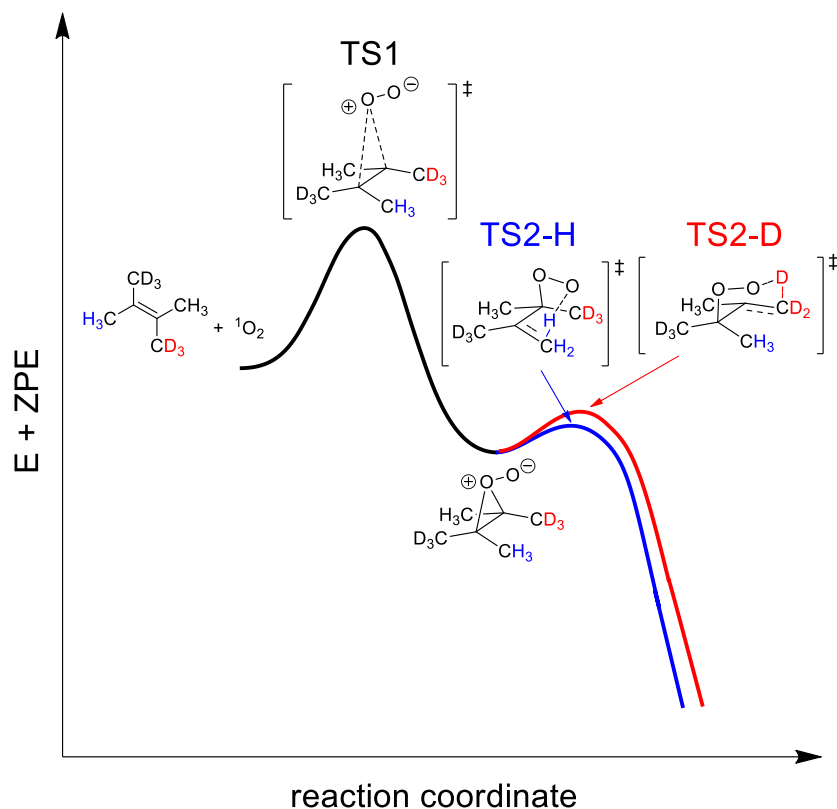


Figure 8. Qualitative reaction coordinate diagram for reaction of **5** with $^1\text{O}_2$.

The substantial intramolecular isotope effects in the ene reaction of triazolinedione with **5** and **6** and the lack of one with **4** also supports an intermediate with a symmetry similar to the perepoxide,^{30b} although the isotope effects are much higher in magnitude than in the ene reaction of singlet oxygen with the same deuterium-labelled substrates.³² This suggests that the extent of allylic C-H bond breaking in the product-determining transition state from the perepoxide to the hydroperoxide product in the singlet oxygen ene reaction must be less advanced than the analogous transition state from the aziridinium imide to its ene product.

In an attempt to quantitatively interpret the KIE results, transition state theory (TST) was used to determine the temperature dependence of these isotope effects assuming that the isotopic perturbation adds roughly 0.20 kcal/mol of zero-point energy to the product-determining barrier (Table 1). Although the isotope effects in every case are consistent with the well-understood qualitative notion that selectivity increases as temperature decreases, the agreement is not quantitative for any of the studied alkenes. Thus, these experiments are not enough to fully support the existence of an intermediate peroxide, so more evidence will have to be provided from computational studies to settle the mechanism.

Computational Studies

Accurately modeling the interaction of $O_2(^1\Delta_g)$, written henceforth as 1O_2 , with organic molecules is a long-standing problem in computational chemistry not only from the standpoint of reproducing experimental reaction kinetics in reactions involving 1O_2 but also in predicting the triplet-singlet energy gap of O_2 . A vacant π^* orbital is left behind as 3O_2 is promoted to its first excited singlet state, which renders the molecule more electrophilic. Although 1O_2 is regarded as a reactive species, the amount of electronic energy gained upon excitation in the gas phase is only 22.4 kcal/mol, which is much smaller than typical bond dissociation energies. For instance, a typical C-H bond has a BDE of ~100 kcal/mol, so in order for a C-H bond cleavage to become spontaneous, other bonding changes must accompany the C-H bond breaking.³³ These bonding changes in a reaction can be modelled using electronic structure calculations to construct a potential energy

surface, which describes how the potential energy of a system varies with molecular geometry.

As a caveat to the ensuing analysis, the single-reference treatment that both restricted DFT and *ab initio* coupled cluster theory provide do not capture the multireference nature of $^1\text{O}_2$ and will therefore overestimate the energy of isolated $^1\text{O}_2$. It is because of this shortcoming that only molecular geometries with a C(alkene)-O distance shorter than 2.00 Å, where the multireference character of the electronic structure is sufficiently low, were chosen to benchmark each of the DFT methods relative to DLPNO-CCSD(T). A correct treatment of the static and dynamic electron correlation present in singlet oxygen necessitates the use of CASPT2 calculations,^{16, 34} but for the sake of simplicity, symmetry-broken unrestricted DFT methods were used to estimate the thermochemistry of the reaction due to the presence of a rate-limiting transition state (TS1) connecting starting materials to the perepoxide that is absent using most restricted DFT methods.

Two methods are typically utilized to determine the best computational model to use for a given system: 1) comparison of experimental observables to those computed with the model and, 2) when experimental data is not available, benchmarking against *ab initio* models known to describe most other systems correctly. Since the perepoxide has not been observed directly for acyclic alkenes, its thermochemistry was estimated using the latter method.

Statistical Models

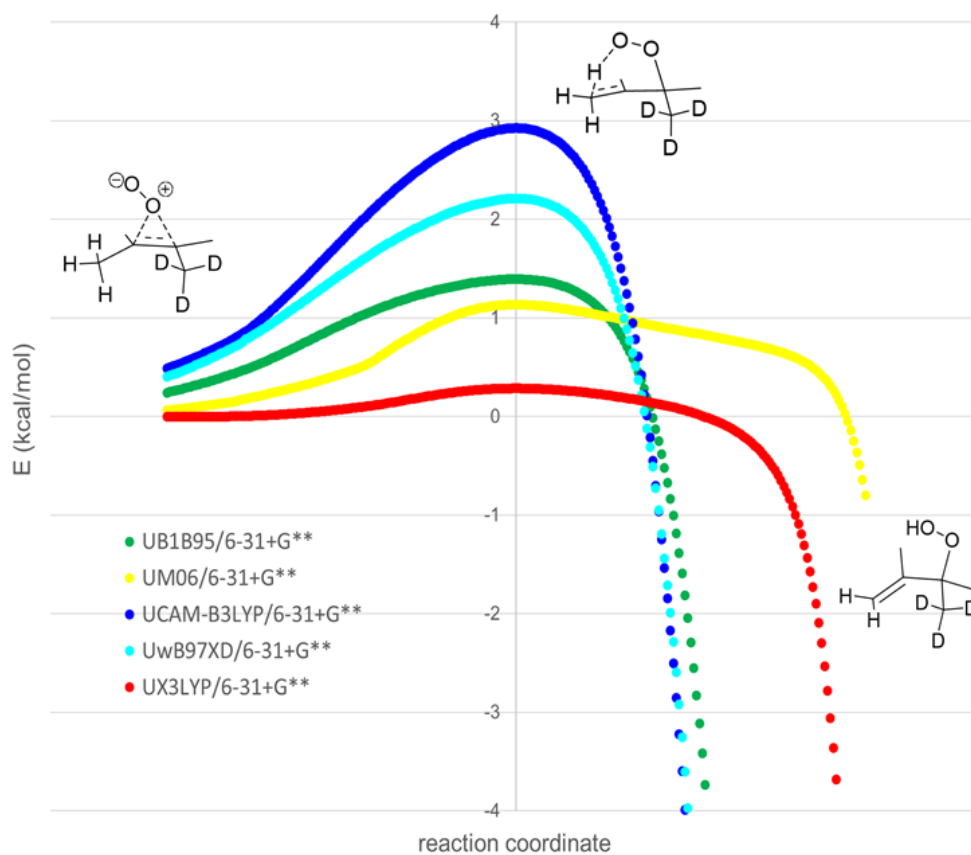


Figure 9. Intrinsic reaction coordinate (IRC) diagrams for the conversion of perepoxide to hydroperoxide using several DFT methods.

A variety of DFT method and basis set combinations were used to calculate the energies of several structures connecting the intermediate perepoxide to the product hydroperoxide, and these energies were compared to those obtained using high-level *ab initio* (DLPNO-CCSD(T)/aug-cc-pvtz) calculations. The potential energy reaction coordinates for the DFT methods with the lowest RMSD from the *ab initio* energies are shown in Figure 9. The IRCs for these closest-matching models span roughly two orders

of magnitude in the product-determining barrier, from one that predicts a modest 3 kcal/mol barrier height and contains a loosely bound intermediate to a model that predicts nearly barrierless (0.6 kcal/mol) hydroperoxide formation.

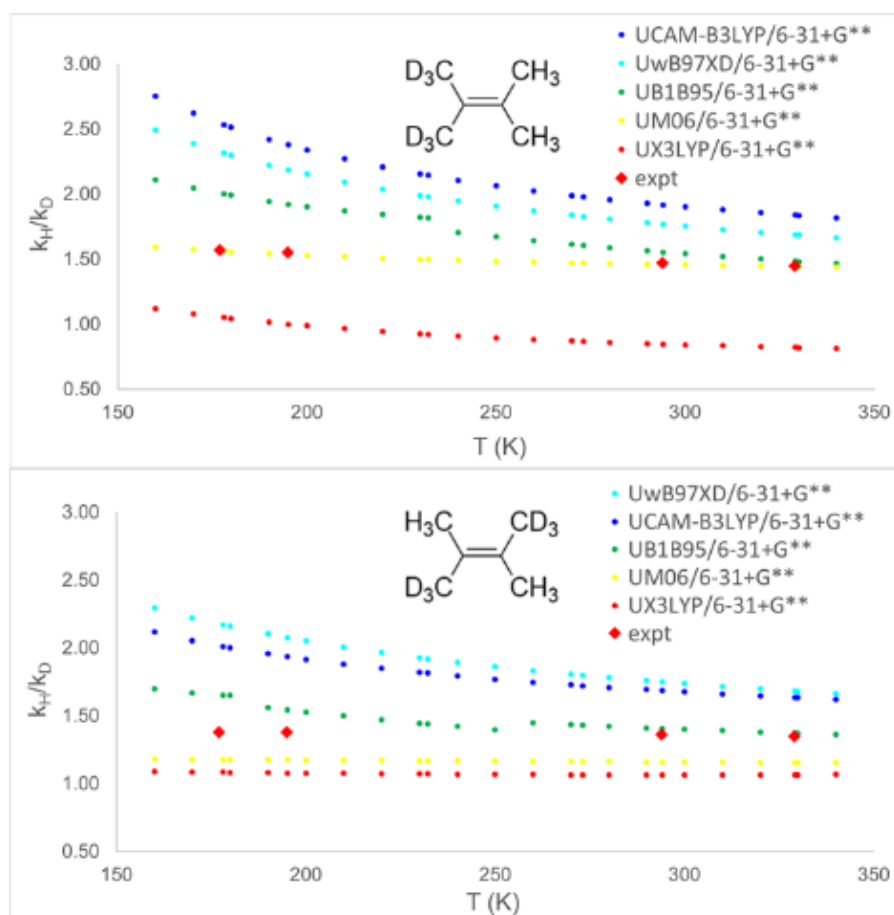


Figure 10. VTST isotope effect predictions and the effect of temperature on the isotopic partitioning.

To determine which of these IRCs could best describe the true potential energy surface of the reaction, variational transition state theory (VTST) was used to predict the intramolecular H/D isotope effects of both **5** and **6** at a range of temperatures (Figure 10).

In simplified terms, variational transition state theory allows for the inclusion of the effects of entropy, ZPE, and temperature on the location of the transition state along the reaction coordinate so that free energy maxima can be located on potential energy surfaces featuring shallow intermediates. For both isotopomers, it is apparent that VTST brings predicted isotope effects closer into agreement with the experimental KIEs (Table 2), but the agreement is not quantitative. There is not a single calculational method among those studied which is able to perfectly predict the KIE results from **5**, **6**, and **7**.

However, the predicted intramolecular H/D KIEs *bracket* the experimental results. Predictions of the isotope effects were made at a range of temperatures that includes the experimental measurements from **5** and **6**. If VTST is applicable to this reaction then the barrier connecting the intermediate to the product is between 0.6-3.0 kcal/mol. Because the conversion from a perepoxide to a hydroperoxide is a first-order unimolecular decomposition, these barrier heights can be translated to intermediate lifetimes between 300 fs and 20 ps. This range of possible lifetimes is consistent with an intermediate that reacts to form the ene product too quickly to undergo competitive ring opening with the cyclopropyl-substituted acyclic alkene studied by Orfanopoulos.²⁸ In the limit of rate-limiting C-H abstraction, the intramolecular isotope effect would be near 7 in the absence of tunneling,³⁵ while as the proton abstraction barrier height diminishes to nothing, VTST predicts that the isotope effect tends towards unity or slightly inverse. The predicted isotope effects are highly sensitive to the height of the barrier and the shape of the potential energy

profile. In effect, the magnitude of the intramolecular KIE in this reaction can be interpreted as a readout of the barrier height for the product-determining step!

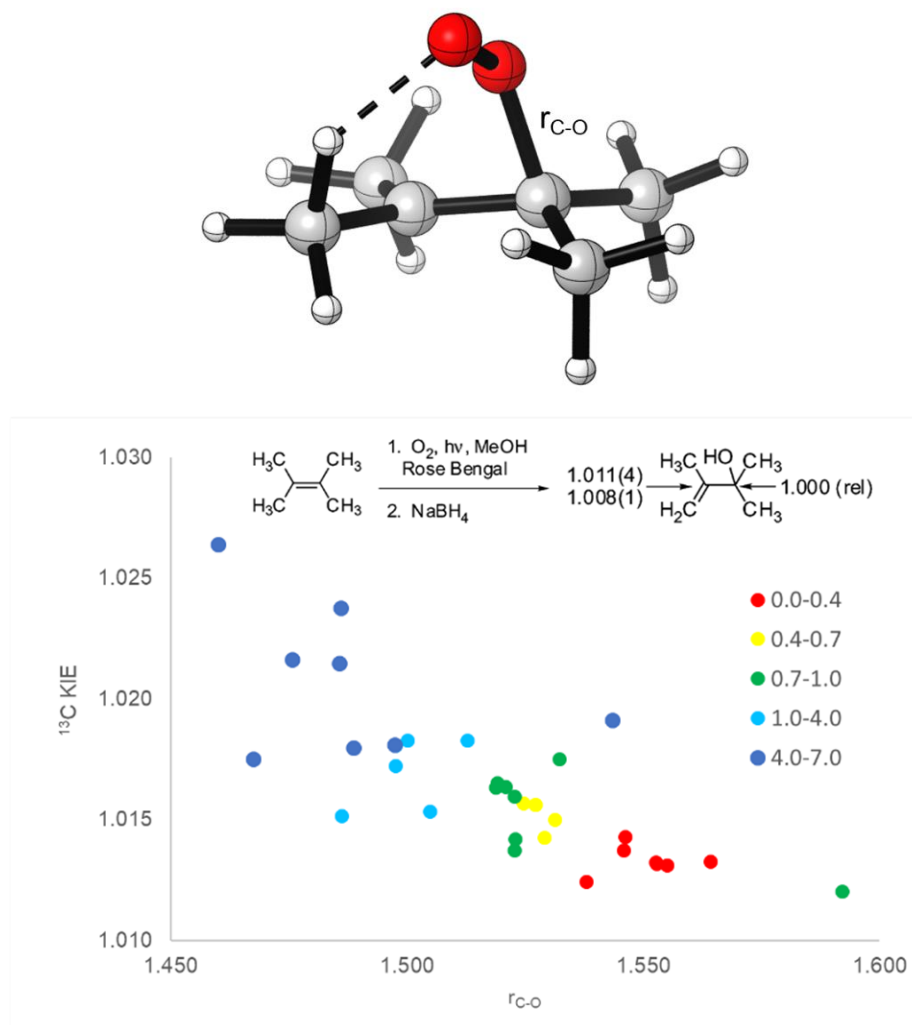


Figure 11. Top: A generalized structure for the proton abstraction transition state from the peroxide intermediate. The developing C-O bond is labelled as r_{C-O} , and a dashed line connects the proton to be abstracted to the terminal oxygen. Bottom: A plot of r_{C-O} versus the QUIVER-predicted intramolecular ^{13}C KIE, with the experimental value for the olefinic carbon shown above. Each data point gives a KIE prediction using a unique DFT method, and the legend is used to describe the potential energy barrier height of the product-determining transition state.

A comparison of calculated and experimental ^{13}C KIEs has been shown to be a good method for establishing an “experimental transition state” and gives accurate transition state structures to within $\pm 0.05 \text{ \AA}$ in critical bond lengths for the epoxidation of 2-methyl-2-butene with 2-(methylsulfonyl)oxaziridine.² A similar study was conducted for the current reaction in an attempt to measure the hydroperoxide C-O bond length ($r_{\text{C-O}}$) in the product-determining transition state indirectly from the ^{13}C intramolecular isotope effect measured in previous work between the two olefinic carbons of TME.^{18a} A total of 41 DFT methods, each of which features a saddle point corresponding to proton abstraction from the perepoxide, were used to make a KIE prediction (Figure 11). There is a clear dependence of the magnitude of the KIE on both $r_{\text{C-O}}$ and product-determining barrier height, but the experimental values (1.008(1) and 1.011(4)) lie beneath every predicted value. While this could result from temperature and entropy changing the location of the product-determining transition state, the lack of agreement shows that the applicability of statistical rate theory to this reaction is suspect.

A mechanistic possibility that is difficult to rule out is the absence of a potential energy barrier connecting the perepoxide and the hydroperoxide, which is tantamount to a true bifurcating surface having two adjacent transition states without an intervening intermediate.^{18a} Although TST cannot be used to predict isotope effects on surfaces of this kind, Lluch has argued that it is possible to do so using VTST.³⁶ To find the VTS on either side of a bifurcating path for the reaction of **5** with $^1\text{O}_2$, Lluch used the NOSADDLE procedure in POLYRATE9.0 to step down the potential energy gradient on both sides of

the VRI. The application of VTST in this way reveals the presence of two dynamical bottlenecks, or free energy transition states, in the bifurcating reaction path that lead to the formation of the two isotopomeric products via two separate rate constants. The KIEs predicted in this way are low compared to experimental values, which suggests that a two-step no-intermediate mechanism cannot be supported by statistical rate calculations. This inconsistency does not rule out other bifurcating surfaces with slightly different topologies.

Other recent computational studies have supported the intermediacy of a perepoxide. Using potentials of mean force (PMF) calculations, Acevedo was able to locate a free energy minimum in the area of the perepoxide, and the depth of the perepoxide well was found to increase with more polar solvents in the simulation.³⁷ Accordingly, the barrier to proton abstraction from the perepoxide was found to increase with solvent polarity from 6.4 kcal/mol in cyclohexane ($\epsilon = 2.0$) to 8.8 kcal/mol in water ($\epsilon = 80.1$), which is consistent with dipole moment attenuation from the charge-separated perepoxide to the chairlike proton abstraction transition state. These barriers are likely to be erroneously high, since they imply a lifetime that is sufficient for ring opening with Orfanopoulos' cyclopropyl-appended alkene.²⁸ Regardless, the impact of the reaction medium on the free energy surface, and by extension the isotope effects, is predicted to be negligible. The effect would be less dramatic than the solvent dependence of the isotope effects seen in triazolinedione ene reactions of **5** and **6**.^{30b}

All current observations are consistent with a perepoxide intermediate that lives on a time scale that is too short for intermolecular trapping with a nucleophile or thermal

equilibration of the surrounding solvent. However, there are physical processes that can occur on the timescale of peroxide decay that compete with reaction and will affect experimental results. Classical experiments performed by Rynbrandt and Rabinovitch have shown that the decomposition of a symmetrical hexafluorobicyclopropyl intermediate, which occurs with a unimolecular rate constant of $3.5 \times 10^{11} \text{ s}^{-1}$, is fast enough to be comparable with the apparent rate constant for intramolecular vibrational redistribution (IVR), which was estimated at $\sim 1.0 \times 10^{12} \text{ s}^{-1}$.³⁸ This physical phenomenon involves the redistribution of excess energy gained in the exothermic generation of an intermediate species, and has been shown to influence the selectivity in other reactions with highly reactive intermediates.³⁹ While a statistical rate theory has been developed to incorporate the effects of this energy relaxation,⁴⁰ nonstatistical treatments may be necessary to better understand this phenomenon.

Trajectory Studies

Since statistical rate theories fail to unambiguously describe the selectivity in these reactions, it is plausible that dynamic trajectories could be used to explain the anomalous selectivity. A preliminary trajectory study was carried out for the reaction of **5** and **6** with $^1\text{O}_2$ to compare the results with predictions from statistical rate theory. To begin to understand the outcome of trajectories, the reaction coordinate must be conceived in a higher dimensionality than the traditional two-dimensional representation shown in Figure 6. A better representation of the potential energy landscape is shown in Figure 12, in which

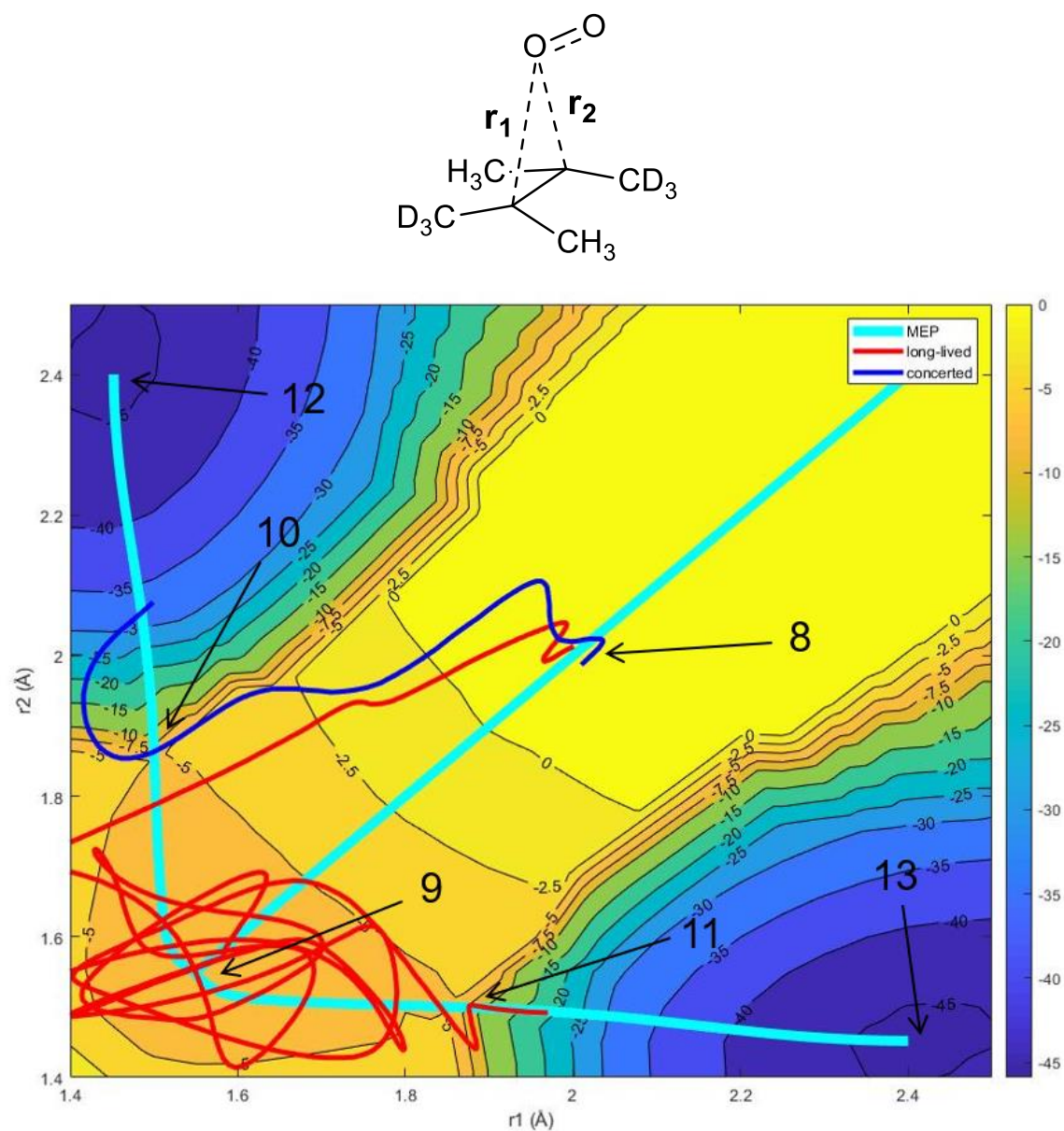


Figure 12. Top: A representative structure for the $^1\text{O}_2/\text{TME}$ system showing the two chosen internal coordinates. Bottom: A potential energy contour plot of the $^1\text{O}_2/\text{TME}$ system with the two C(alkene)-O bond distances plotted in the xy plane and potential energy plotted as contour lines.

two internal coordinates of the $^1\text{O}_2/\text{TME}$ system have been plotted in the x-y plane, and potential energy, calculated using the wB97XD/6-31+G** method and basis set, has been

plotted in the z-dimension as a series of contours. This contour plot shows how the potential energy of the system varies with the two chosen interatomic distances, which are those between the two alkene carbons and the oxygen atom closest to the alkene. These two distances, r_1 and r_2 , are labelled in the representative structure (Figure 12).

The first stage of the minimum energy path (MEP) is a symmetric approach of the $^1\text{O}_2$ bisecting the two alkene carbons that passes through structure **8**. This path ends at a geometry corresponding to the perepoxide intermediate **9**, which resides in a shallow potential energy well. Here the MEP splits in two directions, each of which leads to a transition state (**10** or **11**) that converts the perepoxide to H-abstraction ene product **12** or D-abstraction ene product **13**. The potential energy barrier for the conversion of the perepoxide to the ene product is ~ 2.2 kcal/mol. When zero-point energy (ZPE) is added in, the barrier for abstraction of a deuterium from **5** is ~ 0.2 kcal/mol higher than that for abstraction of a proton, causing a slight tilt of the E+ZPE surface towards the H-abstraction product. The contour diagram does not show this bias towards H-abstraction because it is a potential energy surface and not an E+ZPE surface.

The quasiclassical dynamics trajectories were carried out using ProgDyn on the wB97XD/6-31+G** potential energy surface. Because of the absence of a rate-limiting transition state using this method/basis set, trajectories were initiated near **8**, a symmetric structure uphill from the shallow intermediate ($r_1 = r_2 = 2.00 \text{ \AA}$). Trajectories were propagated forward from this area of the surface until the trajectory terminated in a product

well (**12** or **13**) or until 500 fs passed with no product formation. The number of trajectories that formed **12** or **13** and the corresponding isotope effects are shown in Table 2.

The qualitative trends in these isotope effects are consistent with experimental measurements. For instance, the direction of the temperature dependence of the KIEs calculated from trajectories is consistent with the expectation from transition state theory. A larger proportion of gem-d⁶ (**6**) trajectories finish as the H-abstraction product because the "tilt" towards the H-abstraction well is steeper for the E+ZPE surface of **6** than it is for that of **5**. However, the isotope effects observed in these simulations show a larger temperature dependence than those observed from experiment for both **5** and **6**. The same overlarge temperature dependence is seen in the statistical CVT/SCT predictions from the UwB97XD/6-31+G** POLYRATE calculations. The wB97XD and UwB97XD potential energy surfaces are indistinguishable in the area of the perepoxide intermediate, and the barrier height for the product-determining transition states for each method are the same. From Figure 10, it is clear that the CVT/SCT calculations are predicting a smaller temperature dependence for methods that feature smaller product-determining potential

Table 2. Results of trajectory simulations and CVT/SCT predictions of the intramolecular isotope effects of **5** and **6** at -96°C and 25°C.

olefin	temperature	H-abstraction products (12)	D-abstraction products (13)	KIE from trajectories	UwB97XD/6-31+G** CVT/SCT KIE
trans-d ⁶ (5)	25°C	1711	986	1.36 ± 0.01	1.75
	-96°C	1268	774	1.57 ± 0.01	2.17
gem-d ⁶ (6)	25°C	1119	687	1.59 ± 0.01	1.77
	-96°C	722	492	2.14 ± 0.01	2.31

energy barriers, which suggests that the choice of DFT method used to calculate these trajectories is incorrect.

The largest problem encountered in this preliminary trajectory study is the lack of accuracy in the potential energy surface. In order to be consistent with the gas phase experimental result, ΔH^\ddagger for the rate-determining transition state must be 2.6 kcal/mol.⁴¹ A rate-limiting transition state was not able to be located on the wB97XD/6-31+G** surface, which is supported by a monotonic decrease in the potential energy profile calculated for a series of structures connecting starting materials and perepoxide. The pathway from intermediate to product is an example of a closed-shell system, which is well-described using restricted DFT functionals, while the $^1\text{O}_2$ starting material and ene transition state are open-shell and subject to multireference effects that restricted DFT functionals cannot describe. As a result, the potential energy of $^1\text{O}_2$ is overestimated, and the rate-limiting transition state becomes submerged underneath separated starting materials. Because the separated alkene and $^1\text{O}_2$ are 11.1 kcal/mol uphill from where trajectories were arbitrarily initiated on the wB97XD/6-31+G** surface, it is rare that these trajectories have enough initial kinetic energy to climb uphill to starting materials. It is for this reason that trajectories are only run forwards, but they must be run backwards as well to ensure that the trajectory follows a path from starting materials to product. As a possible solution, unrestricted symmetry-broken DFT methods more accurately model the potential energy surface in the area of the rate-limiting transition state (see Computational Procedures).

Although the kinetic isotope effects calculated from these trajectory simulations do not agree quantitatively with experimental values, it is useful to analyze their behavior to formulate new hypotheses about the influence of dynamic effects on this reaction. Two types of trajectories that were commonly observed among those that afforded ene product are “concerted” and “long-lived”, and a representative trajectory for each type is shown in Figure 12. The long-lived trajectories linger in the intermediate well until they have enough energy in product-forming vibrational modes to overcome the H-abstraction barrier **10** or the slightly higher D-abstraction barrier **11**. Long-lived trajectories finish close to the 500 fs limit, while concerted trajectories finish quickly, typically under ~120 fs. Concerted trajectories take a direct path towards products from the rate-limiting transition state by completing C-O and O-H (or O-D) bond formation in the manner of a concerted, asynchronous pericyclic reaction, and these direct paths bypass intermediate **9**.⁴² In the chemical literature, these concerted trajectories that finish faster than the magnitude of the product-determining barrier would suggest based on transition state theory have been described as “dynamically matched”.⁴³ Recent studies on other systems have shown that product selectivity for dynamically matched versus long-lived trajectories are not necessarily the same, and product ratios can be a weighted aggregate of the individual product ratios determined from trajectories over two or more time regimes.⁴⁴

It is understood that the potential energy surface beyond the initial transition state influences product selectivity,¹⁰ but what features of the surface beyond the transition state influence selectivity the greatest? In this study, the intermediate lies in a relatively flat part

of the energy surface, allowing dynamic matching to have a potentially large influence on the product distribution. One of the possible factors that could control the proportion of trajectories that are subject to dynamic matching is the height of the product-determining barrier. The amount of trajectories that are dynamically matched presumably decreases with larger product-determining barriers, since trajectories aimed directly towards either product well as they pass through the first transition state would have to overcome a larger barrier to complete their motion towards the product. This effect is not accounted for in statistical treatments of reaction kinetics and only arises in dynamic trajectory calculations.

In future work, it would be interesting to systematically study the extent to which dynamic matching contributes to the outcome of trajectories on surfaces with varying product-determining barrier heights. This study has already been done on analytical potential energy surfaces,⁴⁵ but full quasiclassical trajectory calculations such as those presented here have not been performed in a similar manner. This would be a study that nicely parallels the statistical predictions of KIEs that have already been done. Simply understanding the expanded dimensionality of the potential energy surface allows one to appreciate that there are many areas of the surface that trajectories can access that are not on the MEP. Trajectories can show novel behavior that is not apparent when using a geometrically restrictive 2D representation of the reaction coordinate and can explain trends in experimental data that are otherwise intractable.

CHAPTER III

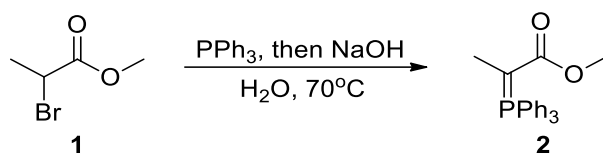
EXPERIMENTAL PROCEDURES

Synthesis Details

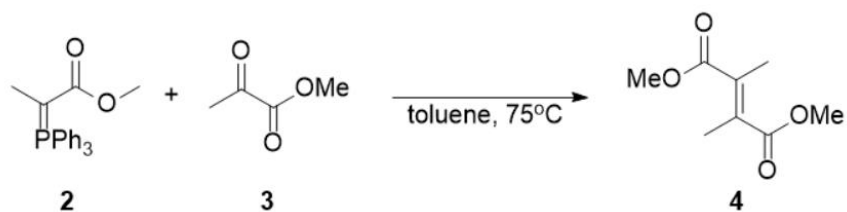
All reactions were performed in oven-dried glassware cooled under a stream of dry N₂ gas prior to use. Flash column chromatography was performed on Silicycle SiliaFlash silica gel F60 (40-63 μm) using the solvent mixtures described in each procedure. Thin layer chromatography (TLC) was performed using Silicycle SiliaPlate (60 Å) glass-backed TLC plates. Compounds were visualized using a 254 nm UV lamp or a stain (KMnO₄, p-anisaldehyde, or bromothymol blue) appropriate for the major functional group in the molecule. Starting materials were purchased from Sigma-Aldrich, BOC Sciences (LiAlD₄), Cambridge Isotope Laboratories, or Oakwood Chemical and used as received. The concentrations of n-butyllithium and methyllithium were determined via titration with menthol using 2,2'-dipyridyl as a colorimetric indicator. THF, diethyl ether, and diglyme were distilled before use under N₂ using Na/benzophenone. Pyridine was distilled from calcium hydride under inert atmosphere before use.

Routine ¹H, ¹³C, and ³¹P NMR spectra were acquired on a Varian 500 MHz or Bruker 400 MHz spectrometer at room temperature. ¹H NMR spectra are referenced to residual CHCl₃ or acetone-d₅ in their respective deuterated solvents, while ¹³C spectra are referenced to the deuterated carbon in each solvent.

Synthesis of tetramethylethylene-*trans*-d⁶

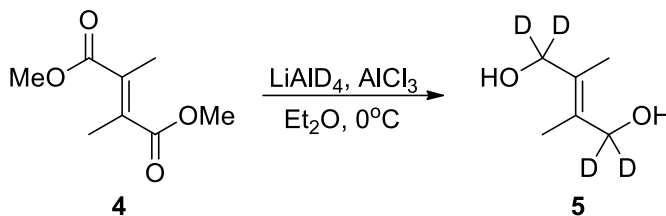


To a suspension of 14.5 g methyl 2-bromopropionate (86.6 mmol) in 180 mL deionized water was added 27.3 g PPh₃ (103 mmol) and the resulting mixture was allowed to react for 12 h at 70°C, after which full conversion of starting material was observed by TLC (eluent = 10% MeOH in CH₂Cl₂). The reaction mixture was cooled to room temperature and 87 mL of a 2 M aqueous solution of NaOH (174 mmol) was added, which resulted in the precipitation of a yellow solid. This aqueous suspension was extracted with three 100 mL portions of CH₂Cl₂. The combined organic extracts were dried with MgSO₄, filtered, and concentrated on a rotatory evaporator to afford a viscous yellow oil. The oil was triturated with 150 mL hexanes, and 28.1 g of the resulting crude yellow solid **2** (80.6 mmol) was used in the next step without further purification. ¹H NMR (CDCl₃, 500 MHz): 1.64-1.58 [3H, ³J_{P-H} (res. 1) = 13.7 Hz, ³J_{P-H} (res. 2) = 14.3 Hz], 3.61 & 3.13 (3H, s), 7.64-7.42 (15H, m).

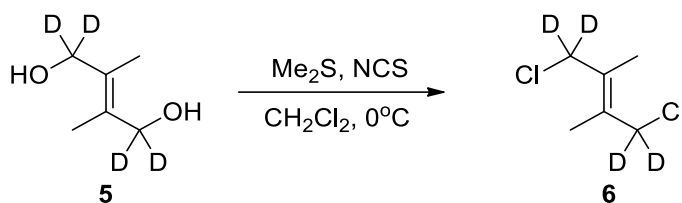


To a solution of 13.1 g ylide **2** (37.6 mmol) in 220 mL toluene was added 4.20 g methyl pyruvate (41.2 mmol) at 75°C, and the mixture was stirred for 20 h at 75°C. The solvent was removed under reduced pressure and the brown residue was subjected to flash

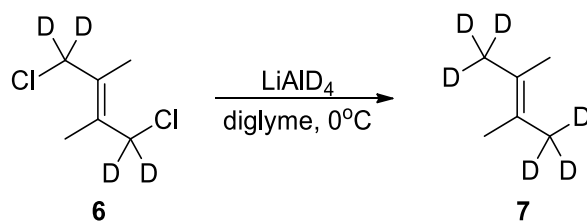
chromatography (1:9 = EtOAc:hexanes) to afford 2.00 g (11.7 mmol) of diester **4** as a white solid. ^1H NMR (CDCl_3 , 500 MHz): 2.05 (3H, s), 3.78 (3H, s).



An ice-cooled solution of 1.91 g AlCl_3 (14.3 mmol) in 50 mL freshly distilled Et_2O was transferred via cannula to an ice-cooled solution of 1.81 g LiAlD_4 (43.0 mmol) in 100 mL Et_2O over a period of 10 min. The resulting suspension was brought to room temperature and stirred for 1 h. The mixture was cooled again to 0°C and a solution of 3.96 g of diester **4** (22.9 mmol) in 80 mL Et_2O was added dropwise over a period of 10 min. After 3h, the starting material was consumed completely by TLC (eluent: 1:1 = EtOAc:hexanes). The reaction was quenched by diluting the mixture with 100 mL Et_2O , cooling to 0°C , then adding sequentially 2 mL water, 2 mL 15% NaOH solution in water, then three additional 2 mL portions of water. After allowing 15 min for the quench, 2 g MgSO_4 was added to the emulsion. After warming to room temperature, the emulsion was passed through a fritted funnel, and the solid material left on the filter was washed with three 50 mL portions of CH_3CN . The mixture of solvents was removed in vacuo to yield 2.28 g of diol **5** (19.0 mmol) as a powdery white solid. The residue was purified via flash column chromatography (eluent: 1:1 = EtOAc:hexanes). ^1H NMR (CDCl_3 , 400 MHz): 1.84 (6H, s); ^{13}C NMR (CDCl_3 , 100 MHz): 15.9, 63.2 (pentet, $^1J_{\text{C-D}} = 21.4$ Hz), 131.6.



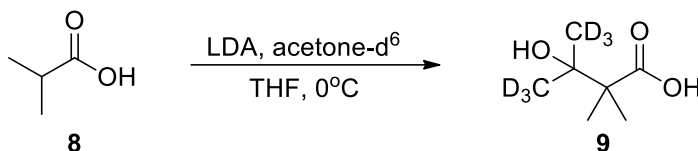
To an ice-cooled solution of 4.99 g recrystallized N-chlorosuccinimide (37.4 mmol) in 190 mL freshly distilled CH_2Cl_2 , 2.79 g Me_2S (44.9 mmol) was added dropwise, resulting in the precipitation of a white solid. 2.25 g of diol **5** (18.7 mmol) was then transferred into the solution as a solid in a single portion. Although the dissolution of the diol occurred slowly, the reaction was complete after stirring at 0°C overnight, which was concurrent with the near disappearance of the precipitate. The reaction mixture was washed with 50 mL ice-cold brine and the aqueous layer was extracted with three portions of 50 mL Et_2O . The organic extracts were combined and the solvents removed under reduced pressure to give a yellow liquid. 5 mL CH_2Cl_2 was added to this isolate and the resulting solution was filtered through a pad of silica using hexanes as eluent. Removing the solvent under reduced pressure yielded 2.14 g of the desired dichloride **6** (13.6 mmol). ^1H NMR (CDCl_3 , 500 MHz): 1.47 (2H, s, broad); 1.90 (6H, s).



In a single portion, 732 mg LiAlD_4 (17.4 mmol) was added to a dry ice/acetonitrile cooled solution of 1.37g dichloride **6** (8.7 mmol) in 45 mL freshly distilled diglyme. The

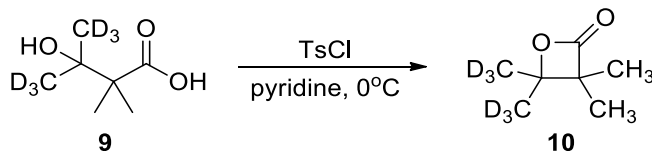
mixture was slowly warmed to 0°C, and the reaction was complete within 3 hours. 425 mg of alkene **7** (5.0 mmol, b.p. = 72°C) was distilled directly from the reaction mixture, which required heating the mixture to 140°C and using a dry ice cooled Hickman still to condense the volatiles. A small amount (~2% relative to **7**) of diglyme was detected in each preparation of **7**. ¹H NMR (acetone-d⁶, 400 MHz): 1.61 (s, 6H); ¹³C NMR (acetone-d⁶, 100 MHz): 20.4, 19.6 (septet, ¹J_{C-D} = 19.2 Hz).

Synthesis of tetramethylethylene-gem-d⁶

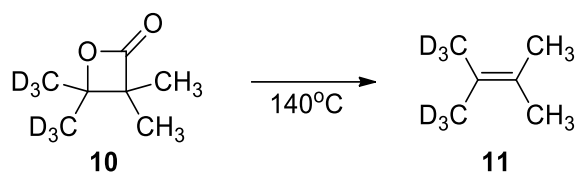


An oven-dried, three-necked 250 mL round bottom flask equipped with an addition funnel was flushed with N₂ and charged with diisopropylamine (12.6 g, 125 mmol) and submerged into a dry ice/acetone bath. 50 mL of a 2.0 M solution of n-butyllithium in hexanes (100 mmol) was added via addition funnel over the course of 30 min while maintaining the internal temperature of the reaction mixture to below -70°C. The mixture was warmed to room temperature and allowed to equilibrate for 30 min. The mixture was cooled again to -78 °C and a solution of 4.40g of **8** (50 mmol) in 50 mL THF was added dropwise over a period of 30 min. After another cycle of warming to room temperature, equilibration for 30 min, and cooling back to -78°C, a solution of 3.84 g acetone-d⁶ (60 mmol) in 25 mL THF was slowly added and the reaction was then stirred under N₂ at 0°C.

After 10 h, conversion of starting material was complete by TLC (1:1 = hexanes:EtOAc), and the reaction mixture was poured into a separation funnel with 100 mL deionized water. The aqueous layer was extracted with three portions of 50 mL Et₂O and acidified to pH 2 with 3 M aqueous HCl solution, resulting in the formation of a white precipitate. The suspension was extracted with three portions of 100 mL Et₂O, then the combined organic extracts were dried with MgSO₄, filtered, and the solvent was removed *in vacuo* to yield 6.83 g of β-hydroxyacid **9** (45 mmol). ¹H NMR (CDCl₃, 400 MHz): 1.25 (s, 6H); ¹³C NMR (CDCl₃, 100 MHz): 21.4, 24.4 (septet, ¹J_{C-D} = 19.2 Hz), 49.6, 73.9, 182.6.

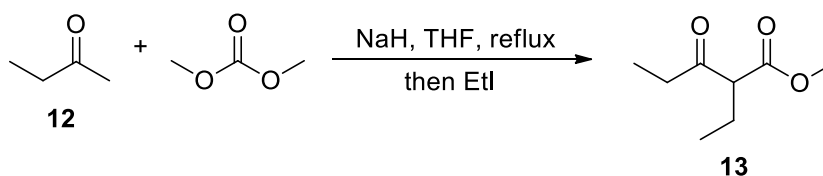


To an ice-cooled solution of 2.30 g of β-hydroxyacid **9** (15 mmol) in 30 mL pyridine was added 5.76 g recrystallized tosyl chloride (30 mmol) with vigorous stirring. The mixture was stirred overnight at 0°C, after which conversion was complete by ¹H NMR. 60 mL deionized H₂O was added slowly while cooling the mixture in an ice water bath. Solid sodium bisulfite monohydrate was then added to the mixture in 500 mg portions until the solution was mildly acidic (pH ~ 4), which resulted in the formation of a white precipitate. The resulting suspension was extracted with three portions of 50 mL Et₂O, the combined organic extracts were dried with MgSO₄, and the solvent was removed on a rotary evaporator to yield 1.31 g of lactone **10** (9.7 mmol) as an off-white solid. ¹H NMR (CDCl₃, 400 MHz): 1.31 (s, 6H).



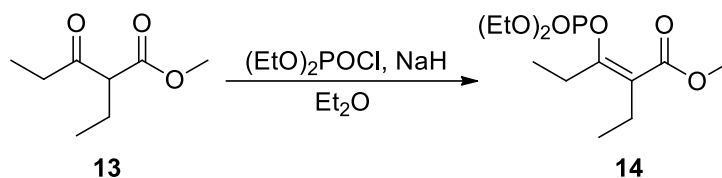
A round bottom flask was charged with 1.00 g lactone **10** (7.4 mmol) and attached to an ice-cooled cold finger trap, which was also connected to an ice-cooled 10 mL receiving flask. The flask was heated to 140°C in an oil bath, upon which the solid began to liquefy and sublime. A heat gun was used to liquefy the sublimed lactone that accumulated on the sides of the reaction vessel. After removing any visible H₂O via microextraction, alkene **11** was carefully distilled over solid Na using a dry ice cooled Hickman still, and 493 mg of purified **11** (5.5 mmol) was collected. ¹H NMR (CDCl₃, 400 MHz): 1.25 (s, 6H); ¹³C NMR (CDCl₃, 100 MHz): 21.4, 24.4 (septet, ¹J_{C-D} = 19.2 Hz), 49.6, 73.9, 182.6.

Synthesis of (Z)-3,4-dimethyl-3-hexene-d³

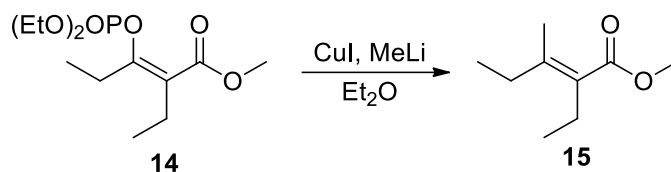


To a solution of 5.77 g ketone **12** (80 mmol) in 160 mL freshly distilled THF, 3.51 g NaH (88 mmol, 60% suspension in mineral oil) was added portionwise and the mixture was brought to reflux. After a 30 min equilibration period, 7.93 g dimethyl carbonate (88 mmol) was added to the refluxing solution. Once ketone **12** was completely consumed, 13.72 g ethyl iodide (88 mmol) was added to the solution and the reaction was continued

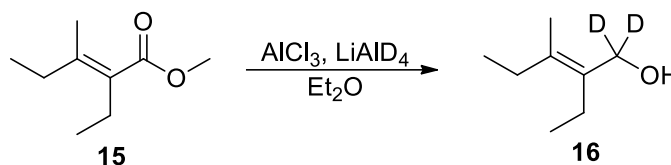
under reflux. After overnight reaction, the mixture was diluted with 150 mL water and extracted with three portions of 150 mL Et₂O. The combined organic extracts were dried over MgSO₄ and concentrated on a rotary evaporator. The crude residue was purified via flash column chromatography (19:1 = hexanes:EtOAc) to yield 5.87 g compound **13** as a colorless oil. ¹H NMR (CDCl₃, 400 MHz): 3.72 (s, 3H), 3.38 (t, ³J_{H-H} = 7.4 Hz, 1H), 2.44-2.64 (m, 2H), 1.84-1.92 (m, 2H), 1.06 (t, ³J_{H-H} = 7.3 Hz, 3H), 0.92 (t, ³J_{H-H} = 7.4 Hz, 3H).



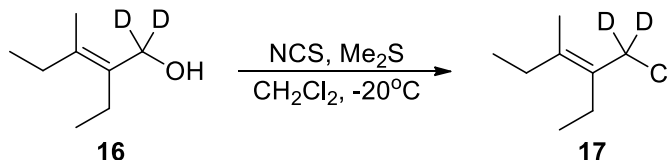
To an oven-dried, nitrogen-flushed round bottomed flask, 5.87 g β -ketoester **13** (37.1 mmol) was dissolved in 80 mL Et₂O, then 1.63 g NaH (40.8 mmol, 60% suspension in mineral oil) was added portionwise to the rapidly stirring solution. After a 30 min equilibration period, 7.04 g diethyl phosphochloridate was added to the mixture, and the reaction proceeded at room temperature overnight. The reaction was quenched with 50 mL 2 M aqueous ammonium chloride, and the aqueous phase was extracted with two additional portions of 100 mL Et₂O. The organic extracts were combined, dried over MgSO₄, and concentrated on a rotary evaporator. The oily residue was purified by flash chromatography (3:2 = hexanes:EtOAc), yielding 7.23 g phosphonate ester **14** as a colorless oil. ¹H NMR (CDCl₃, 400 MHz): 4.13-4.21 (m, 4H), 3.74 (s, 3H), 2.44 (dq, ³J_{H-H} = 7.7 Hz, ⁵J_{P-H} = 1.3 Hz, 2H), 2.28 (dq, ³J_{H-H} = 7.4 Hz, ⁴J_{P-H} = 1.9 Hz, 2H) 1.33 (dt, ⁴J_{P-H} = 1.1 Hz, ³J_{H-H} = 7.0 Hz, 6H), 1.17 (t, ³J_{H-H} = 7.5 Hz, 3H), 1.02 (t, ³J_{H-H} = 7.4 Hz, 3H).



An oven-dried, nitrogen-flushed round bottomed flask was charged with 5.09 g CuI (26.7 mmol) and 100 mL Et₂O. The suspension was cooled in an ice water bath, and 33.4 mL MeLi (53.4 mmol, 1.6 M solution in Et₂O) was added dropwise via addition funnel with rapid stirring. After 1h, the dark brown reaction mixture was cooled to -78°C, then 4.97 g enol phosphate **14** was added dropwise. Reaction progress was monitored via TLC (49:1 = hexanes:EtOAc) until complete conversion of **14** was observed. After 3h, the mixture was slowly warmed to room temperature and quenched with 50 mL saturated NH₄Cl solution. The aqueous layer was extracted with two 100 mL portions of Et₂O, then the organic extracts were combined, dried over MgSO₄, and concentrated on a rotary evaporator. The crude residue was purified via flash column chromatography (49:1 = hexanes:EtOAc), yielding 1.46 g α,β-unsaturated ester **15** as a colorless oil. ¹H NMR (CDCl₃, 400 MHz): 3.73 (s, 3H), 2.30 (qq, ³J_{H-H} = 7.5 Hz, ⁴J_{H-H} = 0.8 Hz, 3H), 2.14 (q, ³J_{H-H} = 7.6 Hz, 3H), 1.92 (t, ⁴J_{H-H} = 0.8 Hz, 3H), 1.03 (t, ³J_{H-H} = 7.5 Hz, 3H), 0.99 (t, ³J_{H-H} = 7.5 Hz, 3H).

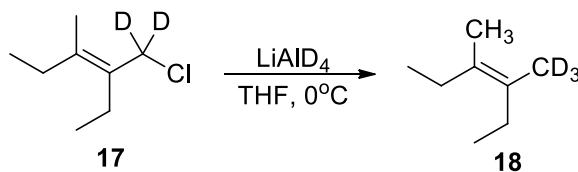


An ice-cooled solution of 642 mg AlCl_3 (4.8 mmol) in 10 mL freshly distilled Et_2O was transferred via cannula to an ice-cooled solution of 606 mg LiAlD_4 (14.4 mmol) in 20 mL Et_2O over a period of 10 min. The resulting suspension was brought to room temperature and stirred for 1 h. The mixture was cooled again to 0°C and a solution of 2.40 g of ester **15** (15.4 mmol) in 30 mL Et_2O was added dropwise over a period of 10 min. After 3h, the starting material was consumed completely by TLC (eluent: 1:9 = EtOAc :hexanes). The reaction was quenched by diluting the mixture with 50 mL Et_2O , cooling to 0°C , then adding sequentially 1 mL water, 1 mL 15% NaOH solution in water, then three additional 1 mL portions of water. After allowing 15 min for the quench, 1 g MgSO_4 was added to the emulsion. After warming to room temperature, the emulsion was passed through a fritted funnel, and the solid material left on the filter was washed with three 30 mL portions of Et_2O . The solvent was removed on a rotary evaporator to yield 1.45 g of allyl alcohol **16** (11.1 mmol) as a powdery white solid. The residue was purified via flash column chromatography (eluent: 1:9 = EtOAc :hexanes). ^1H NMR (CDCl_3 , 400 MHz): 2.15 (qq, $^4J_{\text{H-H}} = 0.7$ Hz, $^3J_{\text{H-H}} = 7.5$ Hz, 2H), 2.06 (q, $^3J_{\text{H-H}} = 7.5$ Hz, 2H), 1.73 (t, $^4J_{\text{H-H}} = 0.7$ Hz, 3H), 0.92-1.62 (s, 1H), 0.99 (m, 6H).



To an ice-cooled solution of 1.15 g recrystallized N-chlorosuccinimide (8.6 mmol) in 25 mL freshly distilled CH_2Cl_2 , 530 mg Me_2S (8.6 mmol) was added dropwise, resulting

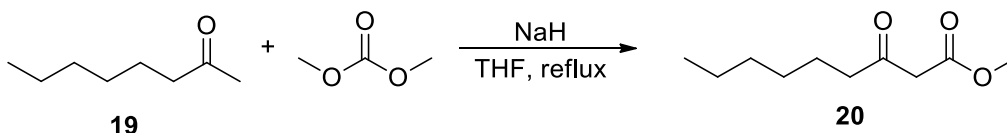
in the precipitation of a white solid. The solution was further cooled to -20°C in a saturated NaCl water/ice solution, then 776 mg of alcohol **16** (8.6 mmol) was then added to the solution in a single portion. The reaction was complete after stirring at 0°C for 3 hours. Upon completion, the reaction mixture was washed with three portions of 20 mL ice-cold brine. The organic extracts were combined and the solvents removed under reduced pressure, ensuring that the temperature of the solution never exceeded 0°C . Removal of solvent yielded 1.16 g of the crude allyl chloride **17** as a colorless oil, which was taken on immediately to the next step without further purification. ^1H NMR (CDCl_3 , 500 MHz): 2.17 (qq, $^4J_{\text{H-H}} = 0.7$ Hz, $^3J_{\text{H-H}} = 7.5$ Hz, 2H), 2.08 (q, $^3J_{\text{H-H}} = 7.5$ Hz, 2H), 1.76 (t, $^4J_{\text{H-H}} = 0.7$ Hz, 3H), 1.01 (t, $^3J_{\text{H-H}} = 7.5$ Hz, 3H), 0.99 (t, $^3J_{\text{H-H}} = 7.5$ Hz, 3H).



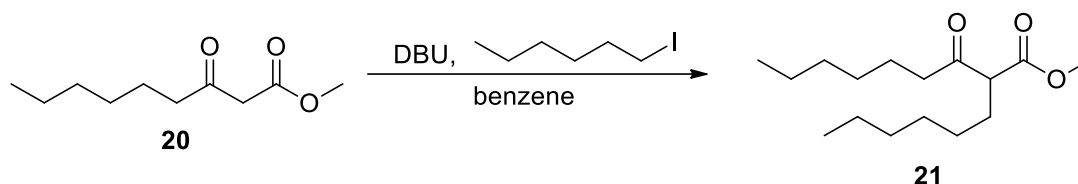
1.16 g of allyl chloride **17** (7.8 mmol) were dissolved with stirring into 40 mL freshly vacuum distilled triglyme in a round-bottomed flask under N_2 , and the solution was cooled in an ice water bath. To the cooled solution, 327 mg lithium aluminum deuteride (7.8 mmol) were added in a single portion. Once the addition was complete, the reaction mixture was slowly warmed to room temperature. Reaction progress was monitored via TLC (100% hexanes), and no starting material was detected after 2 h. The flask was transferred to an oil bath and equipped with a distillation head and cow receiver, and the product was fractionally distilled directly from the reaction mixture

under reduced pressure (bath temperature = 40°C, pressure = 15 Torr). Combining product-containing fractions yielded 377 mg alkene **18** (3.3 mmol) as a colorless liquid. ¹H NMR (CDCl₃, 500 MHz): 2.02 (q, ³J_{H-H}=7.5 Hz, 4H), 1.61 (s, 3H), 0.92-0.97 (m, 6H).

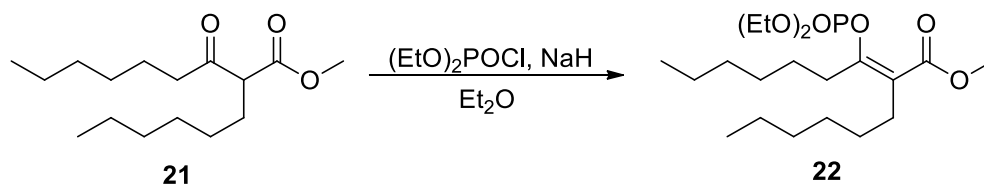
Synthesis of (Z)-7,8-dimethyl-7-tetradecene



An oven-dried, three-necked round-bottom flask equipped with an addition funnel, reflux condenser, and a stir bar was flushed with N₂, then 1.44 g sodium hydride (60 mmol, 60% dispersion in paraffin wax), 6.00 g dimethyl carbonate (67 mmol), and 50 mL toluene were added to the flask. The mixture was heated to reflux, then a solution of 6.41 g **19** (50 mmol) in 10 mL toluene was added dropwise to the refluxing mixture. The reaction was monitored via TLC (eluent: 9:1 = hexanes:EtOAc) using p-anisaldehyde to stain the plate. Once the starting material completely reacted, the mixture was cooled to room temperature and 3.60 g acetic acid (60 mmol) was added dropwise. The resulting mixture was washed with 50 mL ice-cold water, then the layers were separated, and the aqueous layer was extracted with 50 mL EtOAc three times. The combined organic layers were dried over MgSO₄, filtered, and concentrated on a rotary evaporator. The crude residue was purified via silica gel flash column chromatography (9:1 = hexanes:EtOAc) to yield 4.47 g β-ketoester **20** (24 mmol) as a clear, colorless oil. ¹H NMR (CDCl₃, 500 MHz): 3.74 (s, 3H), 3.44 (s, 2H), 2.53 (t, ³J_{H-H} = 7.4 Hz, 2H), 1.51-1.65 (m, 2H), 1.21-1.38 (m, 6H), 0.88 (t, ³J_{H-H} = 7.2 Hz, 3H).

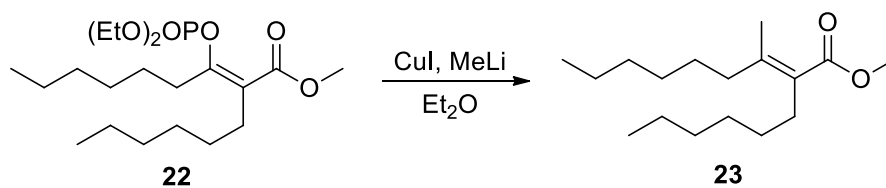


For this step, a modified procedure for alkylation of active methylene compounds was followed.⁴⁶ In a single-necked round-bottom flask, 16.27 g β -ketoester **20** (87 mmol), 14.62 g 1,8-diazabicyclo(5.4.0)undec-7-ene (96 mmol), and 20.36 g 1-iodohexane (96 mmol) were dissolved in 260 mL benzene with magnetic stirring. The mixture was stirred at room temperature overnight, and a white solid slowly precipitated from the solution. The suspension was washed with 100 mL water, then the organic extract was dried over MgSO_4 , filtered, and concentrated to yield a crude yellow oil. The crude product was purified via silica gel flash column chromatography (eluent: 9:1 = hexanes:EtOAc) using p-anisaldehyde stain to visualize the collected fractions on a TLC plate. 9.25 g of compound **21** was received as a clear, colorless oil after removal of volatiles. ^1H NMR (CDCl_3 , 500 MHz): 3.71 (s, 3H), 3.43 (t, $^3J_{\text{H-H}} = 7.3$ Hz, 1H), 2.41-2.57 (m, 2H), 1.75-1.88 (m, 2H), 1.51-1.61 (m, 2H), 1.16-1.36 (m, 14H), 0.82-0.91 (m, 6H).



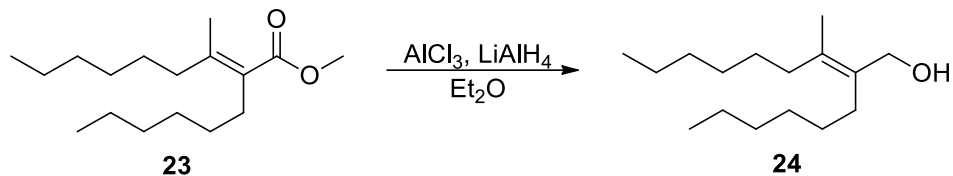
An oven-dried flask equipped with a stir bar and addition funnel was cooled under a stream of N_2 , then 1.17 g NaH (49 mmol, 60% dispersion in paraffin wax) and 30 mL Et_2O were added. A solution of 8.77 g alkylated β -ketoester **21** (32 mmol) in

35 mL Et₂O was added dropwise with stirring, and the evolution of H₂ was observed. Once the addition was complete, the mixture was warmed to room temperature and 8.39 g diethyl phosphorochloridate (49 mmol) was added in one portion. After 2h, the reaction was quenched by adding 30 mL saturated aqueous NH₄Cl. The organic layer was washed with 30 mL saturated NaHCO₃, dried over MgSO₄, filtered, and volatiles were removed on a rotary evaporator. The crude residue was purified via silica gel flash column chromatography (eluent: 80:20 = hexanes:EtOAc), and 8.87 g enol phosphate **22** (23 mmol) was afforded as a viscous oil after combination of pure fractions and removal of solvent. ¹H NMR (CDCl₃, 500 MHz): 4.13-4.21 (m, 4H), 3.74 (s, 3H), 2.41 (dt, ³J_{H-H} = 7.7 Hz, ⁵J_{P-H} = 1.3 Hz, 2H), 2.22-2.27 (dt, ³J_{H-H} = 7.7 Hz, ⁴J_{P-H} = 1.9 Hz, 2H), 1.55-1.63 (m, 2H), 1.34 (dt, ⁴J_{P-H} = 1.1 Hz, ³J_{H-H} = 7.1 Hz, 6H), 1.23-1.44 (m, 14H), 0.85-0.92 (m, 6H).



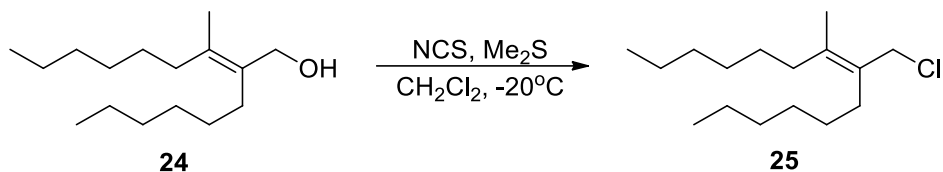
25 mL MeLi (40 mmol, 1.6 M in Et₂O) was added via syringe to an ice-cooled suspension of 3.81 g CuI (20 mmol) in 80 mL Et₂O under N₂. After a one-hour equilibration period, the solution was cooled further to -78°C. 6.25 g enol phosphate **22** (16 mmol) was added to the solution, and the reaction was stirred at -78°C. After three hours, 50 mL saturated aqueous NH₄Cl was poured into the mixture to quench the reaction. The aqueous layer was extracted with 3 x 50 mL Et₂O, then the organic extracts were combined. The organic extracts were washed with 0.1 M NH₄OH, dried over MgSO₄, filtered, and

concentrated *in vacuo*. The crude product was purified via silica gel flash column chromatography (eluent: 49:1 = hexanes:EtOAc) to afford 3.10 g α,β -unsaturated ester **23** (12 mmol) as a colorless oil. $^1\text{H NMR}$ (CDCl_3 , 500 MHz): 3.72 (s, 3H), 2.23-2.29 (m, 2H), 2.06-2.12 (m, 2H), 1.90 (s, 3H), 1.20-1.47 (m, 16H), 0.84-0.93 (m, 6H).

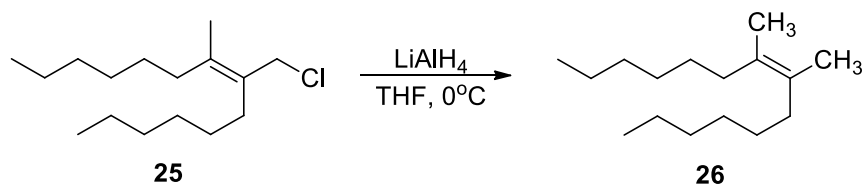


An oven-dried round-bottom flask equipped with a stir bar and a septum was charged with 455 mg LiAlH_4 (12 mmol) and 15 mL Et_2O . The resulting suspension was cooled in an ice water bath and a solution of 1.60 g AlCl_3 (12 mmol) in 10 mL Et_2O was transferred via cannula to the stirring suspension. The mixture was warmed to room temperature and allowed to equilibrate for one hour. After the equilibration period, the mixture was again cooled to 0°C and 1.28 g α,β -unsaturated ester **23** (10 mmol) in 15 mL Et_2O was added dropwise. After three hours, the reaction was quenched by the successive addition of 0.5 mL H_2O , 0.5 mL 15% NaOH , then 1.5 mL H_2O . After 30 minutes of stirring at room temperature, the solution was dried over MgSO_4 , filtered through a pad of Celite, and the filtered solids were washed with three portions of 15 mL Et_2O . The combined organics were concentrated to yield an oily residue. The crude residue was purified via silica gel flash column chromatography (eluent: 49:1 = hexanes:EtOAc), and 1.50 g allyl alcohol **24** (6.3 mmol) was afforded as a clear, colorless oil. $^1\text{H NMR}$ (CDCl_3 , 500 MHz):

4.12 (s, 2H), 2.08-2.14 (m, 2H), 1.99-2.05 (m, 2H), 1.73 (s, 3H), 1.21-1.43 (m, 16H), 1.01 (s, 1H), 0.85-0.93 (m, 6H).



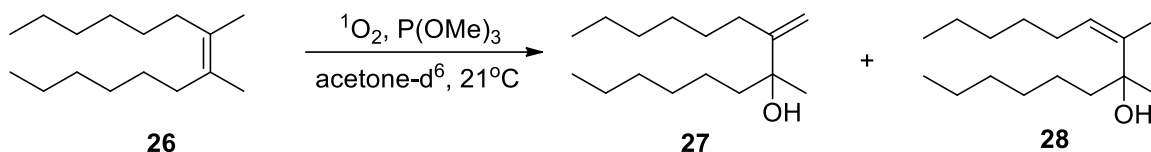
An ice-cooled solution of 881 mg freshly recrystallized N-chlorosuccinimide (6.6 mmol) in 20 mL CH₂Cl₂ was prepared under N₂, and 410 mg Me₂S (6.6 mmol) was added to the stirring solution via syringe. A white solid was observed to precipitate from the solution. After 30 minutes, 1.00 g allyl alcohol **24** (4.1 mmol) was added dropwise, and the solution became clear over the course of 30 minutes at 0°C. 10 mL ice-cold brine was added to the mixture, the layers were separated, and the organic layer was washed twice more with 10 mL ice-cold brine. After removal of volatiles, 1.07 g crude allyl chloride **25** (4.1 mmol) was received as a colorless oil. The crude product was used immediately in the next step without further purification. ¹H NMR (CDCl₃, 500 MHz): 4.12 (s, 2H), 2.10-2.15 (m, 2H), 2.01-2.06 (m, 2H), 1.76 (s, 3H), 1.21-1.43 (m, 16H), 0.85-0.94 (m, 6H).



To a stirring solution of 1.07 g allyl chloride **25** (4.1 mmol) in 20 mL THF cooled in an ice/brine cooling bath was added 157 mg LiAlH₄ (4.1 mmol) in a single portion under N₂. The reaction was warmed to room temperature and allowed to react for two hours, and

GC analysis indicated that conversion of starting material was complete. The reaction was quenched sequentially with 0.2 mL H₂O, 0.2 mL 15% NaOH, and 0.6 mL H₂O, then allowed to stir for 30 minutes. The resulting mixture was filtered over Celite and concentrated on a rotary evaporator, affording a crude oily residue. The product was purified on a long flash chromatography column using silica gel and 100% hexanes as eluent. Combination of pure fractions and concentrating the resulting solution yielded 566 mg alkene **26** (2.5 mmol) as a clear, colorless oil. ¹H NMR (CDCl₃, 500 MHz): 1.93-2.03 (m, 4H), 1.61 (s, 6H), 1.22-1.39 (m, 16H), 9.85-0.94 (t, ³J_{H-H} = 7.1 Hz, 6H).

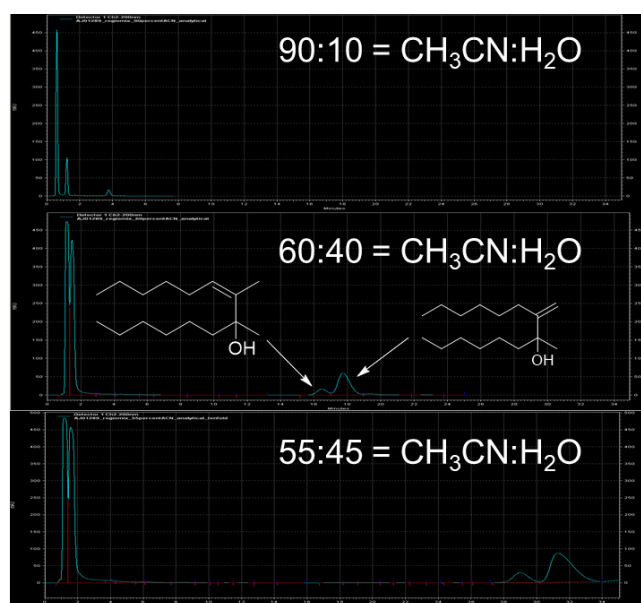
(Z)-7,8-dimethyl-7-tetradecene ¹O₂ Ene Reaction Kinetics

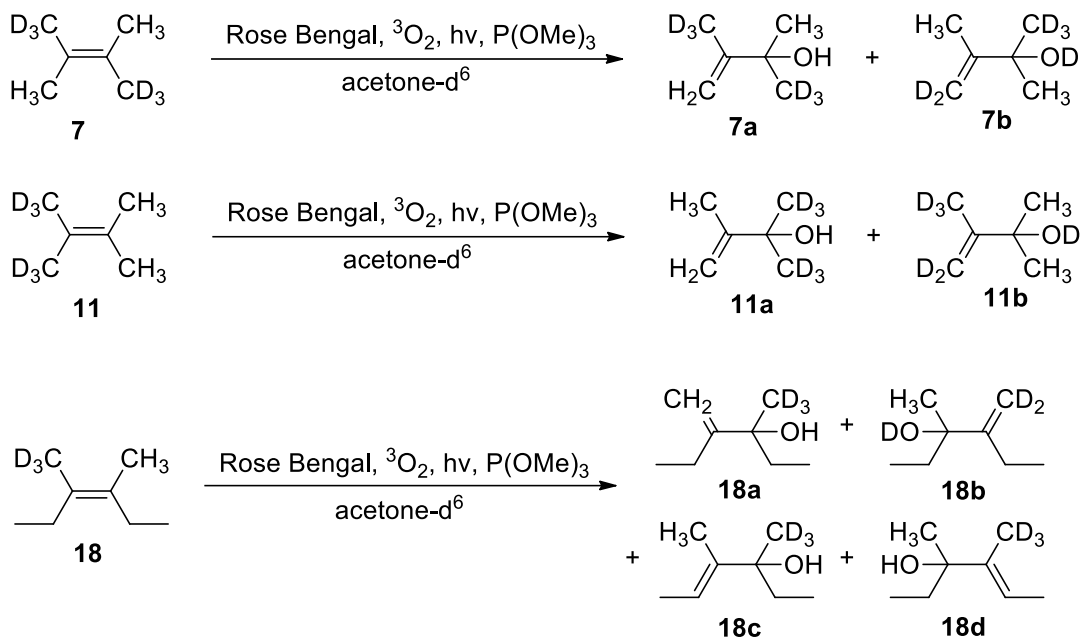


An oven-dried NMR tube capped with a septum was evacuated and backfilled with O₂ three times. The tube was wrapped with aluminum foil and filled sequentially with 22.4 mg (Z)-7,8-dimethyl-7-tetradecene (100 μmol), 24.8 mg freshly distilled P(OMe)₃ (200 μmol), and 200 μL of a 10 mM stock solution of Rose Bengal (2 μmol), then diluted up to 700 μL with acetone-d₆. The reaction was placed under a positive pressure of O₂ with a balloon, then the aluminum sleeve was removed and the solution was irradiated with a 300 W LED bulb.

The progress of the reaction was followed by ¹H NMR to ensure that the product was not decomposing or forming other unwanted side products during the reaction and to later develop a quantitative ¹H NMR technique for the unlabelled product that could be

used to measure the intramolecular isotope effect of the labelled alkene. Two regioisomeric products were detected in the reaction mixture, and the diastereomeric ratio remained constant ($27:28 = 86:14$) over the course of the reaction. Spectral overlap of the carbinol methyl resonance of **28** with the methylene proton resonances in the aliphatic chain of both regioisomers made it difficult to accurately quantitate the carbinol methyl group of the major regioisomer, which is a key resonance for the measurement of the isotope effect of the labelled alkene. The isomers will need to be separated to find a reference integral for the measurement of the isotope effect. A mixture of **27** and **28** was afforded via silica gel flash column chromatography using a Pasteur pipette and hexanes as eluent, and the regioisomers were separated via HPLC on a Shimadzu LC-20AD/T HPLC with a SPD-M20A diode array detector. Each sample was injected onto a Pinnacle DB C18 5 μ analytical column (200 x 1mm). The chromatograms below show the effect of isocratic solvent composition on the efficiency of the separation.



$^1\text{O}_2$ Ene Reaction KIE Procedure

56°C: For each trial, an oven-dried NMR tube was sealed with a rubber septum and charged sequentially with 10 μL tetramethylethylene- d^6 (85 μmol), 200 μL of a 10 mM stock solution of Rose Bengal in acetone- d^6 , and 23 μL freshly distilled $\text{P}(\text{OMe})_3$ (195 μmol). The mixture was diluted to 700 μL with acetone- d^6 , placed into a mineral oil bath heated to 56°C, and introduced to an atmosphere of O_2 via balloon. Once the sample was equilibrated in the temperature bath, it was irradiated with a 300W (4000 lumen) Daylight LED bulb for 6 h. Conversion for each trial is given in the table below, along with raw integrations for each product peak. The temperature of the bath was maintained within $\pm 1^\circ\text{C}$ of the target temperature throughout the course of the reaction. Once the reaction was complete, 20 μL D_2O or H_2O was added to each sample to ensure complete deuterium or proton exchange into the alcohol.

21°C: The samples were prepared exactly as described above, but were irradiated directly at 21°C.

-78°C: The samples were prepared exactly as described above, but were irradiated in an acetone-dry ice temperature bath, which was maintained at a constant temperature of -78 ± 1°C.

-96°C: The samples were prepared exactly as described above but were irradiated in an acetone slurry frozen with liquid N₂. The temperature of the bath was stabilized by periodically adding liquid N₂ throughout the reaction, ensuring that the difference between the measured and target temperature never exceeded 3°C.

KIE Measurement Procedure

Intramolecular H/D kinetic isotope effects were measured using quantitative ¹H NMR spectroscopy. Each ¹H spectrum was acquired using 45 sec delays between calibrated 90° pulses with an acquisition time of 5 sec. In order to validate the qNMR methodology, a standard sample was prepared using unlabeled alkene and subjecting it to the same reaction conditions as detailed above at room temperature. Several spectra were acquired for the standard sample and the deviation of the integrations from values expected for the relative amounts of each chemically equivalent ¹H nucleus never exceeded ±1%. These small changes in relative integrations for each signal did not change the magnitude of the KIEs greatly, so all samples use the same standard integrations for the KIE measurements. The raw integrations were measured using VnmrJ v4.2 with the macro shown below. A first-order baseline correction is implemented in the macro. The only parameters that were

changed from sample to sample were the zero-order (rp) and first-order (lp) phase values in order to ensure that every peak of interest in the spectrum is symmetric.

To minimize the contribution of random error to these high-precision measurements, the reactions were performed six at a time at each temperature. In most cases, the integration of each of the signals corresponding to each isotopomer were divided by the integration of its corresponding peak in the perproteo standard to minimize systematic error and confirm the absence of overlapping impurities. The equations used to calculate the KIEs from the raw integrations are shown below. Standard deviations and 95% confidence intervals were calculated in a standard way. Enough transients were collected to give a signal-to-noise ratio of ~500:1 on the olefinic peaks for each trial, which was particularly important for the low conversion cases.

VNMRJ Macro

```

$mult=1.0
rp=-137.2
lp=2.4
fn=131072
lvl=-0.1
lb=5
wft
#find the center of the first resonance corresponding to isopropyl -CH3 and set it to a chemical shift of 1.2708
sp=607.449 wp=61.43
repeat
  nll('pos',90):$count
  if ($count<1) then th=th-1 endif
  if ($count>1) then th=th+1 endif
  nll('pos',90):$count
until ($count=1)
getll(1):$ht,$freq[1]
cr=$freq[1]
rl(1.2708p)
#now find all of the other peaks and find the frequency at the center of each
sp=4.85p wp=.2p
cr=4.97p
nl nl nl
nl:$ht,$freq[2]
sp=4.55p wp=.2p

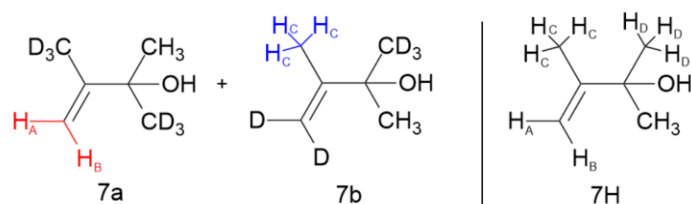
```

```

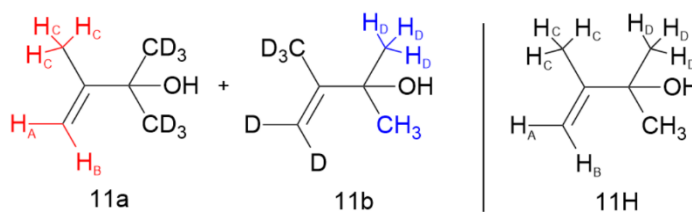
cr=4.67p
nl nl nl
nl:$ht,$freq[3]
sp=1.65p wp=.2p
cr=1.76p
nl nl nl
nl:$ht,$freq[4]
$freq[5]=0.60p #upfield noise region
$freq[6]=5.5p #downfield noise region
sp=1.59p wp=.03p
cr=1.603p
nl nl nl
nl:$ht,$freq[7]
#measure the linewidth at half height for each peak located in the previous section, noting that the lb is set to 5
cz
cr=$freq[1]
dres:$lw1,$res
cr=$freq[2]
dres:$lw2,$res
cr=$freq[3]
dres:$lw3,$res
cr=$freq[4]
dres:$lw4,$res
cr=$freq[7]
dres:$lw7,$res
lb=0
wft
#now mark the regions of the spectrum that will not be included in the first order baseline correction
cz
z(2640,2200)
z(2127,1500)
z(1140,360)
bc(1)
cz
#use all of the previously acquired linewidths and frequencies to cut integrals for each peak one linewidth (at lb=5) from
the center in both directions
z($freq[1]+$lw1*$mult,$freq[1]-$lw1*$mult)
z($freq[2]+$lw2*$mult,$freq[2]-$lw2*$mult)
z($freq[3]+$lw3*$mult,$freq[3]-$lw3*$mult)
z($freq[4]+$lw4*$mult,$freq[4]-$lw4*$mult)
z($freq[5]+$lw4*$mult,$freq[5]-$lw4*$mult)
z($freq[6]+$lw1*$mult,$freq[6]-$lw1*$mult)
z($freq[7]+$lw7*$mult,$freq[7]-$lw7*$mult)
intmod='partial'
is=150000
vs=300
sp=1p
wp=6p
setint(2,1000)
shell('rm ~/vnmrsys/maclib/tempj')
printon
shell('date')
text(file)
nli
printoff('~/vnmrsys/maclib/temp1')
shell('cat ~/vnmrsys/maclib/temp1 >> ~/vnmrsys/maclib/tempj')

```

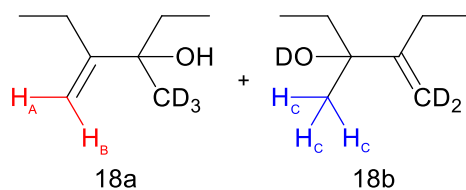
KIE Formulae and Raw Integrations



$$KIE (7) = \frac{k_H}{k_D} = \frac{[7a]}{[7b]} = \frac{(H_{A,7a} + H_{B,7a}) / (H_{A,7H} + H_{B,7H})}{H_{C,7b} / H_{C,7H}}$$



$$KIE (11) = \frac{k_H}{k_D} = \frac{[11a]}{[11b]} = \frac{(H_{A,11a} + H_{B,11a} + H_{C,11a}) / (H_{A,11H} + H_{B,11H} + H_{C,11H})}{H_{D,11b} / H_{D,11H}}$$



$$KIE (18) = \frac{k_H}{k_D} = \frac{[18a]}{[18b]} = \frac{H_{B,18a}}{H_{C,18b}/3}$$

Figure 13. Equations used to calculate the intramolecular kinetic isotope effects for both tetramethylethylene-*trans*-d⁶ (**7**), tetramethylethylene-*gem*-d⁶ (**11**), and 3,4-dimethylhexene-d³ (**18**). The raw integrations used for each product are highlighted in the structure of each isotopomer.

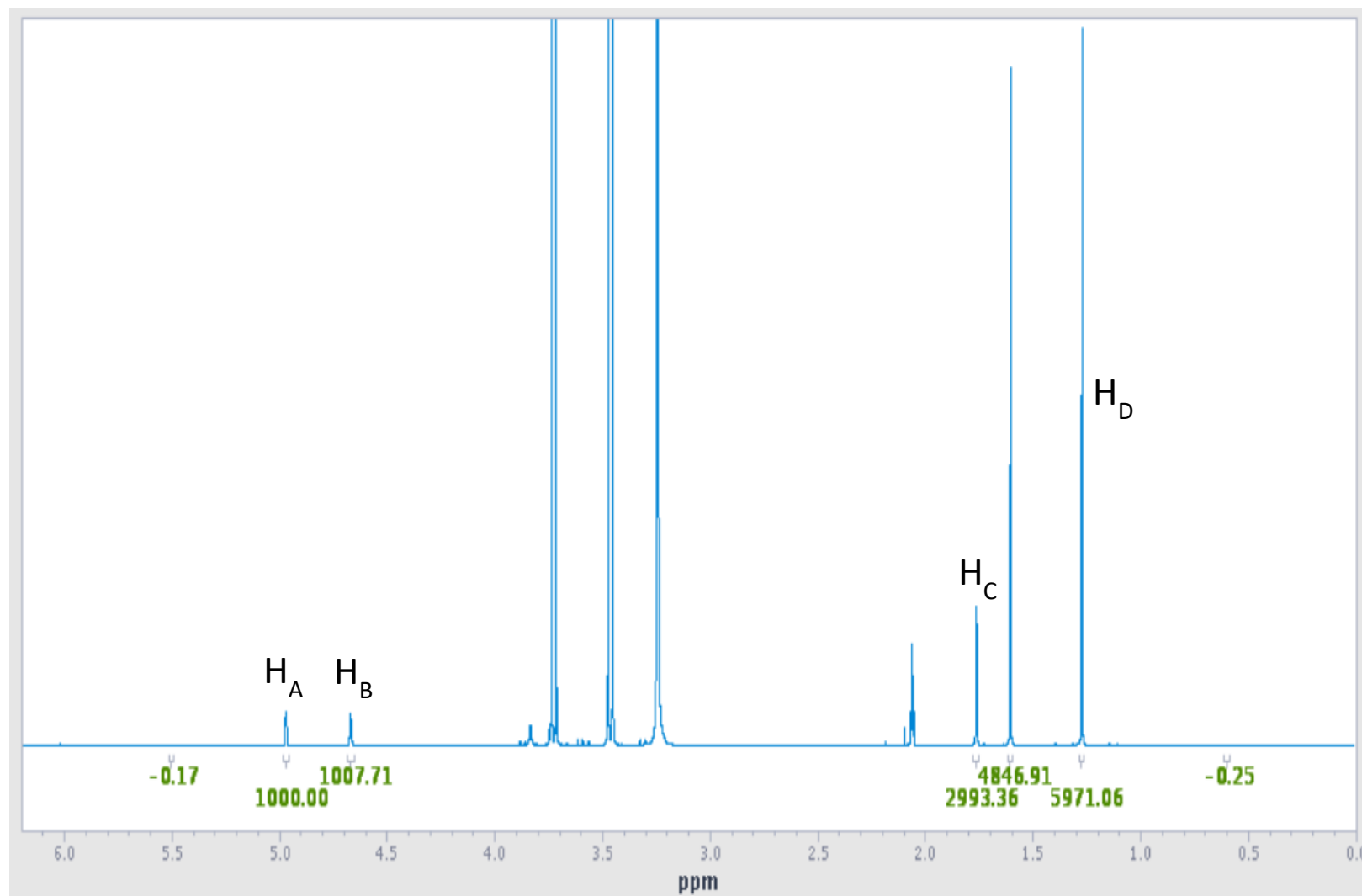


Figure 14. ^1H NMR spectrum of $^1\text{O}_2$ reaction with tetramethylethylene at 55% conversion after application of VNMRJ macro.

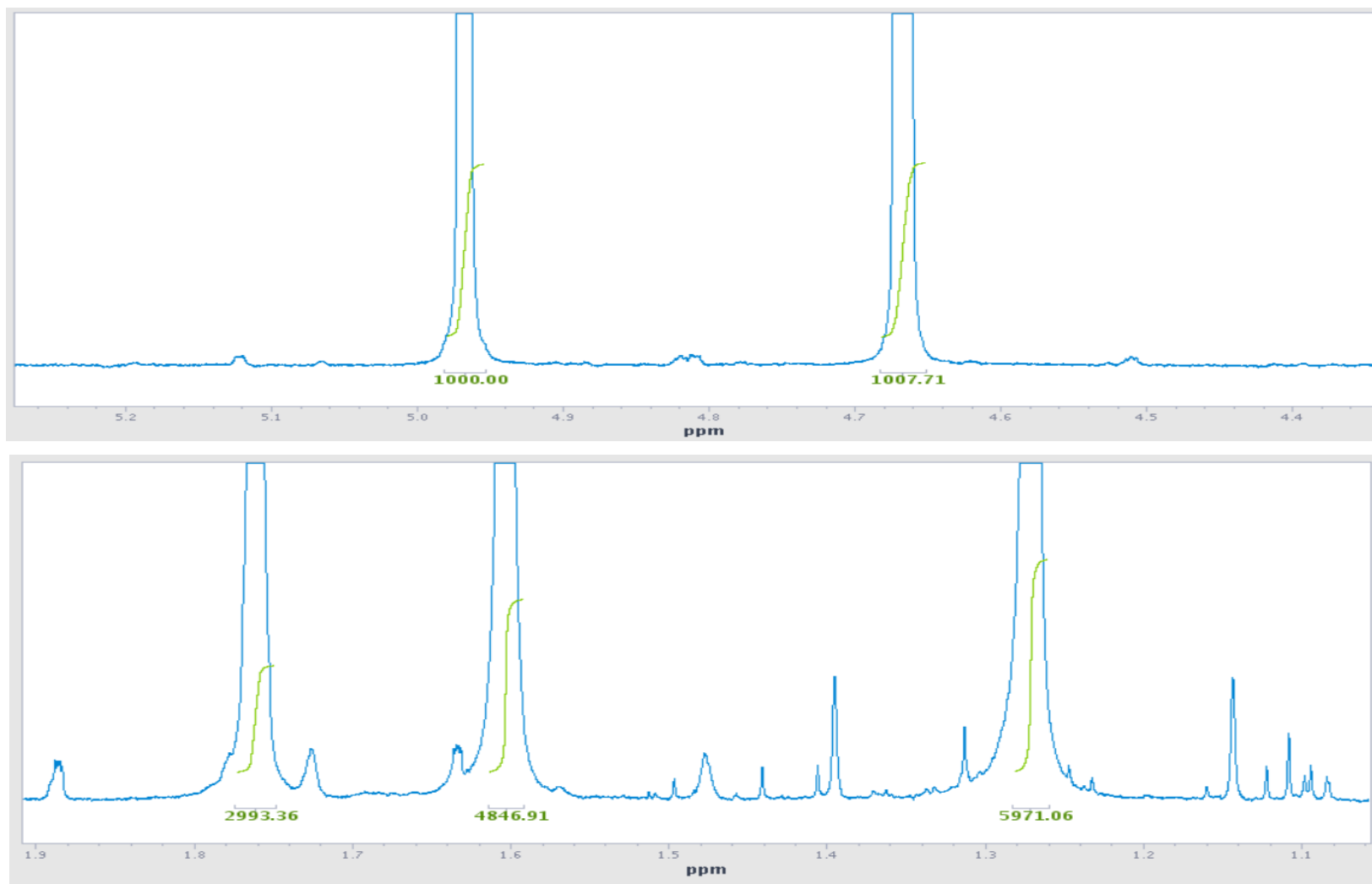


Figure 15. Bottom: Expansion of aliphatic ^1H NMR peaks belonging to tetramethylethylene and allylic alcohol product. Top: Expansion of olefinic peaks between 5.2 and 4.4 ppm.

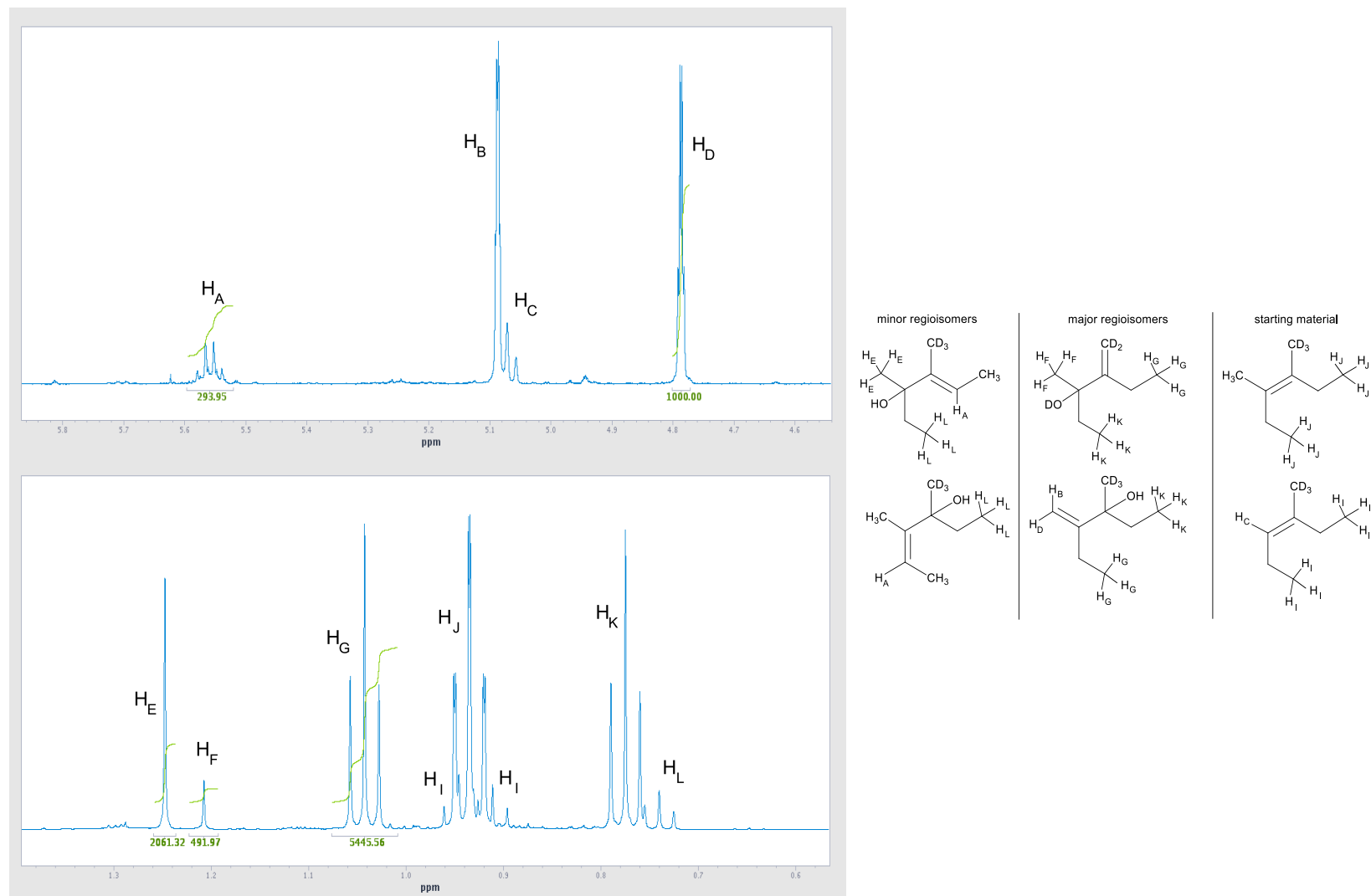


Figure 16. Example ^1H NMR spectrum of $^1\text{O}_2$ ene reaction of 3,4-dimethylhexene- d^3 . All species represented in the spectrum are displayed above. Top: Expansion of olefinic ^1H NMR peaks belonging to major and minor regioisomeric allylic alcohols and starting material contaminant. Bottom: Expansion of aliphatic peaks.

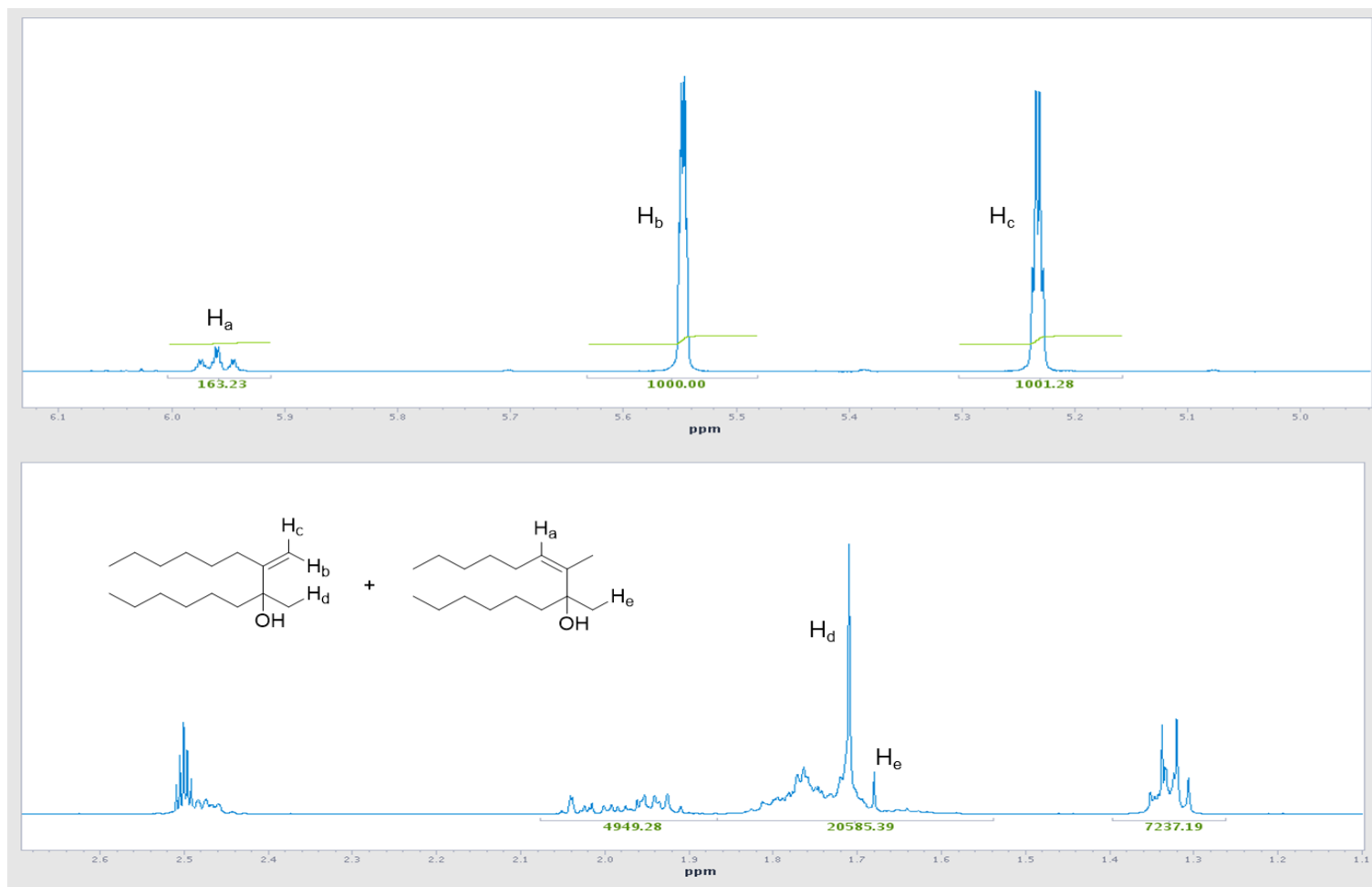


Figure 17. ^1H NMR of mixture of regioisomeric mixture of alcohols resulting from the $^1\text{O}_2$ ene reaction of (Z)-7,8-dimethyl-7-tetradecene. H_d and H_e overlap with the methylene protons in the aliphatic chain, rendering quantitation difficult.

Table 3. Raw integrations and calculated kinetic isotope effects for the singlet oxygen ene reaction of tetramethylethylene-*trans*-d⁶.

temp (°C)	sample	alkene C-H downfield	alkene C-H upfield	vinyllic CH ₃	trans-d6 TME	isopropyl - CH ₃	KIE	% conv
	proteo std	1000	1007.712	2993.361	4846.907	5971.061	-	55
56	trial1	1000	1005.246	2215.551	28.773	5206.932	1.349	100
	trial2	1000	1004.155	2213.263	83.007	5194.218	1.350	99
	trial3	1000	1004.628	2216.264	84.753	5221.089	1.349	99
	trial4	1000	1001.657	2233.672	10702.94	5297.649	1.336	36
	trial5	1000	1006.503	2216.383	495.227	5192.360	1.350	92
	trial6	1000	1003.101	2220.560	5397.123	5198.430	1.345	53
21	trial1	1000	1002.983	2204.378	1460.739	5191.070	1.355	80
	trial2	1000	1005.182	2206.409	130.905	5181.439	1.355	98
	trial3	1000	1003.493	2211.483	98.842	5254.751	1.351	98
	trial4	1000	1005.72	2203.066	2520.866	5188.638	1.357	70
	trial5	1000	1003.355	2203.476	99.875	5248.620	1.356	98
	trial6	1000	1003.358	2204.817	0	5192.216	1.355	100
-78	trial1	1000	1005.18	2158.781	8922.362	5136.445	1.385	40
	trial2	1000	999.416	2163.215	16348.42	5136.320	1.378	27
	trial3	1000	1002.168	2162.981	12903.87	5161.834	1.380	32
	trial4	1000	1001.425	2161.228	10002.34	5147.111	1.381	37
	trial5	1000	1003.062	2165.613	20122.29	5169.593	1.379	23
	trial6	1000	1002.131	2158.924	16330.04	5138.928	1.383	27
-96	trial1	1000	1001.148	2161.683	6961.011	5136.631	1.380	46
	trial2	1000	1004.732	2176.492	7105.449	5191.900	1.373	46
	trial3	1000	1001.065	2160.927	6176.006	5140.023	1.381	49
	trial4	1000	998.391	2161.926	6477.703	5123.980	1.378	48
	trial5	1000	1003.822	2165.442	6185.98	5144.736	1.380	49
	trial6	1000	1005.261	2175.395	8262.678	5155.864	1.374	42

Table 4. Raw integrations and calculated kinetic isotope effects for the singlet oxygen ene reaction of tetramethylethylene-*gem*-d⁶.

temp (°C)	sample	alkene C-H downfield	alkene C-H upfield	vinylic CH ₃	gem-d6 TME	isopropyl - CH ₃	KIE	% conv
	proteo std	1000	1007.712	2993.361	4846.907	5971.061	-	55
56	trial1	1000	1047.087	3001.894	6945.918	4124.903	1.461	46
	trial2	1000	1010.238	2991.84	656.605	4103.213	1.456	90
	trial3	1000	1006.321	2998.962	5380.65	4118.723	1.451	53
	trial4	1000	1038.206	3006.299	6556.127	4129.438	1.459	48
	trial5	1000	1004.692	3004.928	2405.053	4123.871	1.450	71
	trial6	1000	1012.636	3005.376	3096.561	4126.206	1.452	66
21	trial1	1000	1016.354	3002.828	136.021	4058.262	1.477	98
	trial2	1000	1018.818	2999.795	187.236	4056.229	1.477	97
	trial3	1000	1007.899	2997.837	477.352	4052.884	1.475	93
	trial4	1000	1008.314	3004.078	542.118	4068.650	1.471	92
	trial5	1000	1003.506	2999.046	78.932	4065.016	1.469	99
	trial6	1000	1003.948	3003.451	191.388	4067.879	1.470	97
-78	trial1	1000	1003.891	3004.722	12494.84	3837.202	1.558	32
	trial2	1000	1021.252	3006.241	8427.809	3841.067	1.563	42
	trial3	1000	1011.46	3008.634	11269.08	3847.998	1.558	35
	trial4	1000	1010.392	3010.09	20430.35	3861.027	1.552	23
	trial5	1000	1011.063	3004.749	15151.74	3867.703	1.548	28
	trial6	1000	1003.891	3004.722	12494.84	3837.202	1.558	32
-96	trial1	1000	1017.902	2994.857	31804.62	3799.529	1.575	16
	trial2	1000	1011.116	3003.816	11910.81	3811.207	1.571	33
	trial3	1000	1030.098	2995.174	33406.65	3785.516	1.585	15
	trial4	1000	1047.833	3006.976	18965.09	3808.477	1.585	24
	trial5	1000	1029.954	3000.915	11221.02	3836.881	1.565	35

Table 5. Raw integrations and calculated kinetic isotope effects for the singlet oxygen ene reaction of 3,4-dimethylhexene-d³.

temp (°C)	sample	minor alkene C-H	major alkene C-H upfield	SM vinylic CH ₃	major PDT CH ₃ unreacted	minor PDT CH ₃ unreacted	major PDT CH ₃ chain terminus	KIE	% conv
56	trial1	370.815	1000	9084.602	2092.214	563.811	2750.305	1.434	42
	trial2	366.491	1000	9959.713	2072.565	555.699	2696.711	1.447	40
	trial3	373.454	1000	9995.08	2063.597	558.307	2706.16	1.454	40
	trial4	363.5	1000	6313.171	2074.15	566.232	2779.894	1.446	51
	trial5	350.103	1000	2257.806	2053.234	540.760	2651.526	1.461	74
	trial6	359.826	1000	6882.536	2065.063	549.581	2655.565	1.453	48
21	trial1	293.946	1000	4962.217	2061.325	491.973	5445.556	1.455	71
	trial2	281.108	1000	5331.804	2076.928	491.659	5473.185	1.444	69
	trial3	276.645	1000	7092.717	2076.983	474.650	5530.305	1.444	63
	trial4	201.887	1000	11175.82	2089.4	319.280	2743.472	1.436	35
	trial5	295.21	1000	5208.87	2096.966	506.534	5368.531	1.431	69
	trial6	222.826	1000	14792.401	2078.373	327.073	2783.949	1.443	30
-78	trial1	157.451	1000	10866.31	1947.565	294.399	2735.565	1.540	36
	trial2	162.336	1000	10908.57	1926.284	293.566	2708.089	1.557	35
	trial3	174.372	1000	8988.818	1921.854	292.343	2656.209	1.561	40
	trial4	171.888	1000	10336.2	1923.939	285.632	2654.586	1.559	36
	trial5	173.825	1000	10037.35	1938.946	289.292	2649.787	1.547	37
	trial6	170.063	1000	9017.391	1927.878	284.496	2626.545	1.556	39

Calculational Procedures

All molecular geometries and their associated potential energies were calculated using standard procedures for locating stationary points in Gaussian09.⁴⁷ Vibrational frequency analysis was performed on all located stationary points and used to predict KIEs using QUIVER.⁴⁸ Of the 50 symmetry-broken unrestricted DFT methods that were studied in combination with the 6-31+G** basis set, 41 were found to have a structure corresponding to a perepoxide intermediate in the gas phase. The intramolecular ¹³C KIEs predicted from the proton abstraction transition state are shown in Table 4. IRCs and intramolecular CVT/SCT KIEs were calculated from the highlighted methods using POLYRATE (Figure 8).⁴⁹ In all cases, the 6-31+G** basis set was used. Geometric coordinates of the structures used in these calculations can be found in the Appendix for the highlighted methods.

Table 6. DFT methods used to model the decomposition of the perepoxide intermediate and their corresponding barrier heights, developing C-O bond lengths, and intramolecular olefinic ¹³C KIEs. The methods highlighted in red were used to calculate the IRCs and VTST KIEs in Figures 8 and 9.

DFT method	r _{C-O} (Å)	PE barrier height (kcal/mol)	olefinic ¹³ C KIE
UAPF	1.531	0.5	1.015
UAPFD	1.538	0.3	1.012
UB1B95	1.505	1.4	1.015
UB1LYP	1.523	0.8	1.014
UB2PLYPD3	1.592	0.9	1.012
UB3LYP	1.564	0.1	1.013
UB3P86	1.555	0.2	1.013
UB3PW91	1.553	0.2	1.013
UB971	1.554	1.0	1.006

UB972	1.529	0.5	1.014
UB98	1.546	0.2	1.014
UBHandH	1.460	4.4	1.026
UBHandHLYP	1.468	7.0	1.018
UBMK	1.486	3.5	1.015
UCAM-B3LYP	1.498	2.9	1.018
UHFS	1.836	23.3	1.000
UHISSbPBE	1.476	4.3	1.022
UHSEH1PBE	1.527	0.6	1.016
ULC-wPBE	1.486	5.4	1.021
UM05	1.532	0.9	1.018
UM052X	1.497	4.5	1.003
UM06	1.513	1.1	1.018
UM062X	1.486	5.4	1.024
UM06HF	1.465	9.2	1.023
UM06L	1.530	0.4	1.000
UM11	1.497	4.7	1.018
UMP2	1.595	16.6	1.012
UmPW1LYP	1.523	0.7	1.014
UmPW1PBE	1.519	0.8	1.017
UmPW1PW91	1.519	0.8	1.016
UmPW2PLYP	1.543	4.7	1.019
UmPW3PBE	1.553	0.2	1.013
UN12SX	1.500	1.5	1.018
UOHSE1PBE	1.527	0.6	1.016
UOHSE2PBE	1.525	0.7	1.016
UPBE1PBE	1.521	0.8	1.016
UPBEh1PBE	1.523	0.8	1.016
USOGGA11X	1.489	4.2	1.018
UVSXC	2.205	1.5	1.003
UwB97XD	1.498	2.2	1.017
UX3LYP	1.546	0.3	1.014

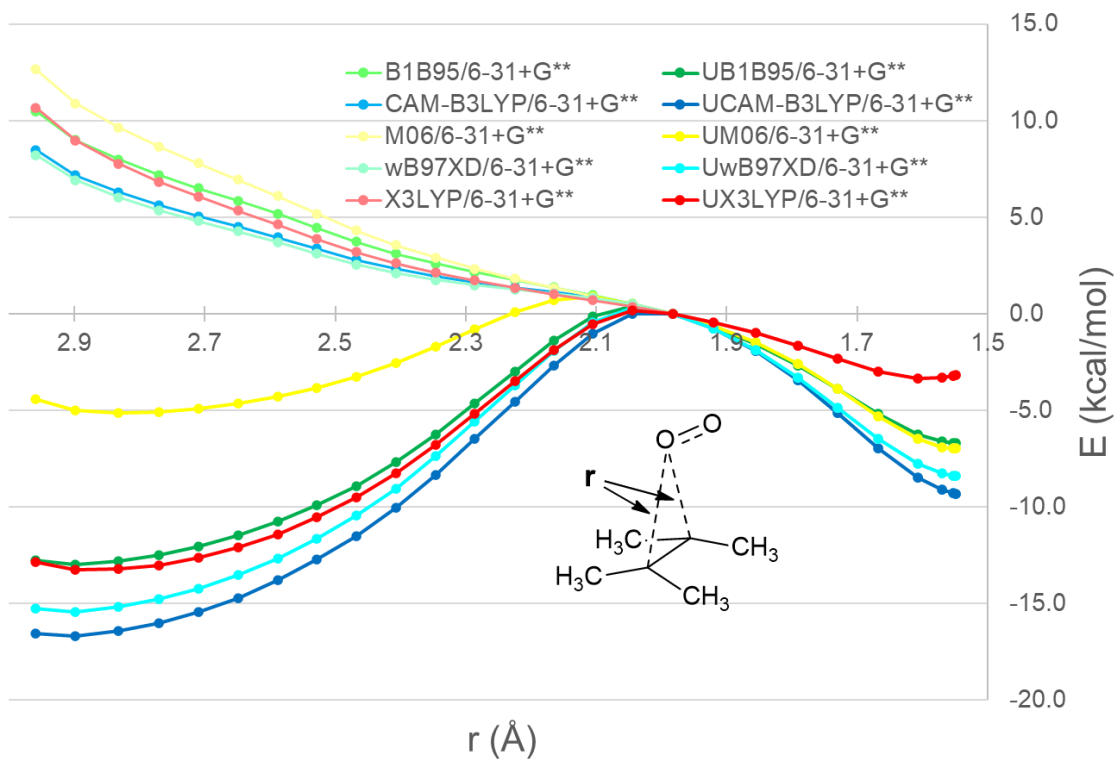


Figure 18. Potential energy profiles connecting starting materials to intermediate for several DFT method/basis set combinations.

Figure 17 shows the potential energy profiles along the pathway between separated $^1\text{O}_2/\text{TME}$ and perepoxide that were calculated using restricted DFT methods and their symmetry-broken unrestricted counterparts. For symmetry-broken unrestricted DFT energies, the keyword `guess=mix` was used in the route line of the Gaussian09 input file. The restricted and unrestricted potential energy profiles for each DFT method become indistinguishable after the plots pass through where the potential energy was arbitrarily set to zero. This point ($r = 2.0 \text{ \AA}$) is also where quasiclassical trajectories were initiated. Based on these apparent barrier heights, UM06/6-31+G** has the closest match to the

experimental enthalpy of activation of 2.2 kcal/mol, assuming the potential energy closely approximates enthalpy along this path. With the correct unrestricted DFT method in hand, it will be possible to understand the nature of the regiochemistry of these reactions in future studies.

CHAPTER IV

CONCLUSION

In this work, a major shortcoming of statistical rate theories in making quantitative predictions of reaction selectivity was illustrated. Transition state theory provided a testable hypothesis and the experimental results are not consistent with the predictions. The measurement of a small temperature dependence on the intramolecular isotope effects for **5**, **6**, and **7** was not able to be exactly reproduced by using statistical rates calculated from isotopomeric transition states. Several computational methods were explored, and none were able to exactly reproduce experimental results despite the tight range of intermediate lifetimes used to model them.

Chemistry still has not come far enough to accurately predict the outcome of reactions that are influenced by nonstatistical dynamics on a bifurcating (or nearly bifurcating) surface. While statistical rate theories can provide relative rate constant predictions that are close to experimentally measured isotope effects for the $^1\text{O}_2$ ene reaction with **5** and **6**, the agreement is not quantitative for both isotopomers. However, this study provides a good starting point for future work by providing reliable kinetic isotope effects at a large range of temperatures and computational models that are nearly consistent with experiments and feature a short-lived peroxide intermediate that is not detectable using typical physical organic probes.

REFERENCES

1. Bigeleisen, J.; Mayer, M. G., *J. Chem. Phys.* **1947**, *15*, 261-267.
2. Hirschi, J. S.; Takeya, T.; Hang, C.; Singleton, D. A., *J. Am. Chem. Soc.* **2009**, *131*, 2397-2403.
3. Truhlar, D. G.; Garrett, B. C., *Acc. Chem. Res.* **1980**, *13*, 440-448.
4. Carpenter, B. K., *Reactive Intermediate Chemistry*. John Wiley & Sons, Inc.: 2004.
5. Valtazanos, P.; Ruedenberg, K., *Theor. Chim. Acta* **1986**, *69*, 281-307.
6. Herman, M. S.; Goodman, J. L., *J. Am. Chem. Soc.* **1988**, *110*, 2681-2683.
7. a) Ess, D. H.; Wheeler, S. E.; Iafe, R. G.; Xu, L.; Celebi-Olcum, N.; Houk, K. N., *Angew. Chem. Int. Edit.* **2008**, *47*, 7592-7601; b) Hare, S. R.; Tantillo, D. J., *Pure Appl. Chem.* **2017**, *89*, 679-698.
8. a) Celebi-Olcum, N.; Ess, D. H.; Aviyente, V.; Houk, K. N., *J. Org. Chem.* **2008**, *73*, 7472-7480; b) Ussing, B. R.; Hang, C.; Singleton, D. A., *J. Am. Chem. Soc.* **2006**, *128*, 7594-7607; c) Wang, Z.; Hirschi, J. S.; Singleton, D. A., *Angew. Chem. Int. Ed. Engl.* **2009**, *48*, 9156-9; d) Bekele, T.; Christian, C. F.; Lipton, M. A.; Singleton, D. A., *J. Am. Chem. Soc.* **2005**, *127*, 9216-9223; e) Merrer, D. C.; Doubleday, C., *J. Phys. Org. Chem.* **2011**, *24*, 947-951; f) Lopez, R. V.; Faza, O. N.; Lopez, C. S., *J. Org. Chem.* **2017**, *82*, 4758-4765; g) Chen, S. M.; Yu, P. Y.; Houk, K. N., *J. Am. Chem. Soc.* **2018**, *140*, 18124-18131.
9. Caramella, P.; Quadrelli, P.; Toma, L., *J. Am. Chem. Soc.* **2002**, *124*, 1130-1131.
10. Thomas, J. B.; Waas, J. R.; Harmata, M.; Singleton, D. A., *J. Am. Chem. Soc.* **2008**, *130*, 14544-14555.

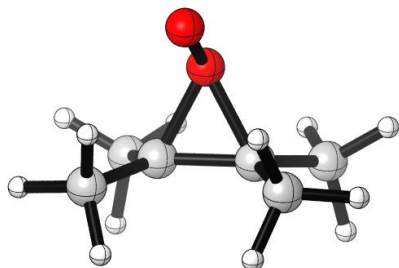
11. a) Weitman, M.; Major, D. T., *J. Am. Chem. Soc.* **2010**, *132*, 6349-6360; b) Siebert, M. R.; Manikandan, P.; Sun, R.; Tantillo, D. J.; Hase, W. L., *J. Chem. Theory Comput.* **2012**, *8*, 1212-1222; c) Siebert, M. R.; Zhang, J. X.; Addepalli, S. V.; Tantillo, D. J.; Hase, W. L., *J. Am. Chem. Soc.* **2011**, *133*, 8335-8343; d) Hong, Y. J.; Tantillo, D. J., *Nat. Chem.* **2009**, *1*, 384-389.
12. a) Bogle, X. S.; Singleton, D. A., *Org. Lett.* **2012**, *14*, 2528-2531; b) Itoh, S.; Yoshimura, N.; Sato, M.; Yamataka, H., *J. Org. Chem.* **2011**, *76*, 8294-8299.
13. Wolf, L. M.; Thiel, W., *J. Org. Chem.* **2014**, *79*, 12136-12147.
14. Hare, S. R.; Tantillo, D. J., *Chemical Science* **2017**, *8*, 1442-1449.
15. Carpenter, B. K., *Chem. Rev.* **2013**, *113*, 7265-86.
16. Borden, W. T.; Hoffmann, R.; Stuyver, T.; Chen, B., *J. Am. Chem. Soc.* **2017**, *139*, 9010-9018.
17. Foote, C. S.; Wexler, S., *J. Am. Chem. Soc.* **1964**, *86*, 3879-&.
18. a) Singleton, D. A.; Hang, C.; Szymanski, M. J.; Meyer, M. P.; Leach, A. G.; Kuwata, K. T.; Chen, J. S.; Greer, A.; Foote, C. S.; Houk, K. N., *J. Am. Chem. Soc.* **2003**, *125*, 1319-1328; b) Singleton, D. A.; Hang, C.; Szymanski, M. J.; Greenwald, E. E., *J. Am. Chem. Soc.* **2003**, *125*, 1176-1177.
19. a) Hurst, J. R.; Schuster, G. B., *J. Am. Chem. Soc.* **1982**, *104*, 6854-6856; b) Hurst, J. R.; Wilson, S. L.; Schuster, G. B., *Tetrahedron* **1985**, *41*, 2191-2197.
20. Kopecky, K. R.; Vandesan.Jh, *Canadian Journal of Chemistry-Revue Canadienne De Chimie* **1972**, *50*, 4034-4049.
21. Grdina, S. B.; Orfanopoulos, M.; Stephenson, L. M., *J. Am. Chem. Soc.* **1979**, *101*, 3111-3112.

22. Dai, S.-H.; Dolbier, W. R., Jr., *J. Am. Chem. Soc.* **1972**, *94*, 3946-52.
23. Dolbier, W. R.; Dai, S. H., *J. Am. Chem. Soc.* **1970**, *92*, 1774-&.
24. a) Orfanopoulos, M.; Grdina, S. M. B.; Stephenson, L. M., *J. Am. Chem. Soc.* **1979**, *101*, 275-276; b) Schulteelte, K. H.; Muller, B. L.; Rautenstrauch, V., *Helv. Chim. Acta.* **1978**, *61*, 2777-2783.
25. Houk, K. N.; Williams, J. C.; Mitchell, P. A.; Yamaguchi, K., *J. Am. Chem. Soc.* **1981**, *103*, 949-951.
26. a) Stratakis, M.; Orfanopoulos, M., *Tetrahedron* **2000**, *56*, 1595-1615; b) Stratakis, M.; Orfanopoulos, M., *Tetrahedron Lett.* **1995**, *36*, 4291-4294; c) Orfanopoulos, M.; Stratakis, M.; Elemes, Y., *Tetrahedron Lett.* **1989**, *30*, 4875-4878.
27. Poon, T. H. W.; Pringle, K.; Foote, C. S., *J. Am. Chem. Soc.* **1995**, *117*, 7611-7618.
28. Alberti, M. N.; Orfanopoulos, M., *Org. Lett.* **2008**, *10*, 2465-2468.
29. Newcomb, M.; Chestney, D. L., *J. Am. Chem. Soc.* **1994**, *116*, 9753-9754.
30. a) Grdina, M. B.; Orfanopoulos, M.; Stephenson, L. M., *J. Org. Chem.* **1979**, *44*, 2936-8; b) Vougioukalakis, G. C.; Roubelakis, M. M.; Alberti, M. N.; Orfanopoulos, M., *Chem. - Eur. J.* **2008**, *14*, 9697-9705.
31. a) Bharti, S. K.; Roy, R., *Trac-Trends in Analytical Chemistry* **2012**, *35*, 5-26; b) Monakhova, Y. B.; Diehl, B. W. K., *Magnetic Resonance in Chemistry* **2017**, *55*, 996-1005; c) Pauli, G. F.; Jaki, B. U.; Lankin, D. C., *Journal of Natural Products* **2007**, *70*, 589-595.
32. Cheng, C. C.; Seymour, C. A.; Petti, M. A.; Greene, F. D.; Blount, J. F., *J. Org. Chem.* **1984**, *49*, 2910-2916.

33. Turro, N. J. R., V.; Scaiano, J. C., *Modern Molecular Photochemistry of Organic Molecules*. University Science Books: 2010.
34. Borden, W. T.; Davidson, E. R., *Acc. Chem. Res.* **1996**, *29*, 67-75.
35. Westheimer, F. H., *Chem. Rev.* **1961**, *61*, 265-273.
36. Gonzalez-Lafont, A.; Moreno, M.; Lluch, J. M., *J. Am. Chem. Soc.* **2004**, *126*, 13089-13094.
37. Sheppard, A. N.; Acevedo, O., *J. Am. Chem. Soc.* **2009**, *131*, 2530-40.
38. Rynbrandt, J. D.; Rabinovitch, B. S., *J. Phys. Chem.-Us* **1970**, *74*, 4175.
39. a) Quijano, L. M.; Singleton, D. A., *J. Am. Chem. Soc.* **2011**, *133*, 13824-7; b) Bailey, J. O.; Singleton, D. A., *J. Am. Chem. Soc.* **2017**, *139*, 15710-15723.
40. Zheng, J. J.; Papajak, E.; Truhlar, D. G., *J. Am. Chem. Soc.* **2009**, *131*, 15754-15760.
41. Ashford, R. D.; Ogryzlo, E. A., *J. Am. Chem. Soc.* **1975**, *97*, 3604-3607.
42. Chen, Z.; Nieves-Quinones, Y.; Waas, J. R.; Singleton, D. A., *J. Am. Chem. Soc.* **2014**, *136*, 13122-5.
43. Carpenter, B. K., *Angew. Chem. Int. Ed.* **1998**, *37*, 3341-3350.
44. Roytman, V. A.; Singleton, D. A., *J. Am. Chem. Soc.* **2020**, *142*, 12865-12877.
45. Collins, P.; Carpenter, B. K.; Ezra, G. S.; Wiggins, S., *J. Chem. Phys.* **2013**, *139*, 154108.

46. Ono, N.; Yoshimura, T.; Saito, T.; Tamura, R.; Tanikaga, R.; Kaji, A., *B. Chem. Soc. Jpn.* **1979**, *52*, 1716-1719.
47. *Gaussian 09, Revision A.02*, M. J. Frisch, G. W. T., H. B. Schlegel, G. E. Scuseria, M. A. Robb, J. R. Cheeseman, G. Scalmani, V. Barone, G. A. Petersson, H. Nakatsuji, X. Li, M. Caricato, A. Marenich, J. Bloino, B. G. Janesko, R. Gomperts, B. Mennucci, H. P. Hratchian, J. V. Ortiz, A. F. Izmaylov, J. L. Sonnenberg, D. Williams-Young, F. Ding, F. Lipparini, F. Egidi, J. Goings, B. Peng, A. Petrone, T. Henderson, D. Ranasinghe, V. G. Zakrzewski, J. Gao, N. Rega, G. Zheng, W. Liang, M. Hada, M. Ehara, K. Toyota, R. Fukuda, J. Hasegawa, M. Ishida, T. Nakajima, Y. Honda, O. Kitao, H. Nakai, T. Vreven, K. Throssell, J. A. Montgomery, Jr., J. E. Peralta, F. Ogliaro, M. Bearpark, J. J. Heyd, E. Brothers, K. N. Kudin, V. N. Staroverov, T. Keith, R. Kobayashi, J. Normand, K. Raghavachari, A. Rendell, J. C. Burant, S. S. Iyengar, J. Tomasi, M. Cossi, J. M. Millam, M. Klene, C. Adamo, R. Cammi, J. W. Ochterski, R. L. Martin, K. Morokuma, O. Farkas, J. B. Foresman, and D. J. Fox Gaussian, Inc.: Wallingford, CT, 2009.
48. Saunders, M.; Laidig, K. E.; Wolfsberg, M., *J. Am. Chem. Soc.* **1989**, *111*, 8989-8994.
49. *POLYRATE*, Zheng, J. Z., S.; Lynch, B. J.; Corchado, J. C.; Chuang, Y.-Y.; Fast, P. L.; Hu, W.-P.; Liu, Y.-P.; Lynch, G. C.; Nguyen, K. A.; Jackels, F.; Ramos, A.; Ellingson, B. A.; Melissas, V. S.; J.; Rossi, Coitino, E. L.; Pu, J.; Albu, T. V.; Steckler, L.; Garrett, B. C.; Isaacson, A. D.; Truhlar, D. G. Minneapolis, MN, 2010.

APPENDIX

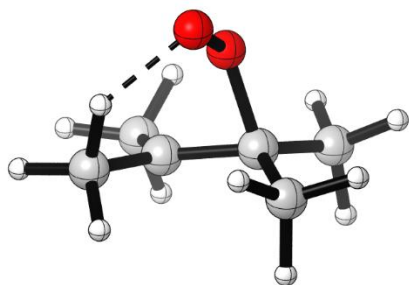


1O2tme_INTtoPDT_UM06_6-31+Gdp_gasphaseIRC_INT.log
 E(UM06) = -385.907708214

Zero-point correction= 0.169569 (Hartree/Particle)
 Thermal correction to Energy= 0.179679
 Thermal correction to Enthalpy= 0.180623
 Thermal correction to Gibbs Free Energy= 0.135459
 Sum of electronic and ZPE= -385.738139
 Sum of electronic and thermal Energies= -385.728030
 Sum of electronic and thermal Enthalpies= -385.727085
 Sum of electronic and thermal Free Energies= -385.772249

	E	CV	S
	KCal/Mol	Cal/Mol-K	Cal/Mol-K
Total	112.750	37.291	95.055

C,0,1.9598284051,0.8702054226,-0.2432025291
 C,0,0.8169393131,0.0168549357,0.2134735707
 C,0,-0.5604621887,0.5433667523,0.3166080771
 C,0,1.1806014126,-1.2372099835,0.9358853632
 C,0,-1.5669356677,-0.1869839736,1.1414852493
 C,0,-0.8953520011,1.9614926877,-0.0294043433
 H,0,1.6578950691,1.6703079565,-0.9219339707
 H,0,2.6984430983,0.2468780679,-0.7585024464
 H,0,2.4517838765,1.3203707477,0.6282841531
 H,0,0.6104695128,-2.0546741788,0.4657951995
 H,0,0.9182892953,-1.190277315,1.9979400469
 H,0,2.2507589802,-1.444177047,0.8474272642
 H,0,-1.2043470873,-0.379664363,2.1565557935
 H,0,-1.7513290166,-1.151756456,0.6419786754
 H,0,-2.5037275821,0.3737587972,1.2038749431
 H,0,-0.2289592341,2.3928492116,-0.7789650004
 H,0,-0.8478287858,2.5801680683,0.8756558699
 H,0,-1.9194329759,2.0116709531,-0.4146122231
 O,0,-0.1599017159,-0.2316088191,-0.9710055823
 O,0,-0.6646037077,-1.5233274646,-1.1159991106



1O2me_INTtoPDT_UM06_6-31+Gdp_gasphaseIRC_TS2.log
E(UM06) = -385.905901706

Zero-point correction= 0.168953 (Hartree/Particle)
Thermal correction to Energy= 0.178443
Thermal correction to Enthalpy= 0.179387
Thermal correction to Gibbs Free Energy= 0.135439
Sum of electronic and ZPE= -385.736949
Sum of electronic and thermal Energies= -385.727459
Sum of electronic and thermal Enthalpies= -385.726514
Sum of electronic and thermal Free Energies= -385.770463

	E	CV	S
	KCal/Mol	Cal/Mol-K	Cal/Mol-K
Total	111.975	35.285	92.497

C,0,1.9325927563,1.0347476551,-0.1364128746
C,0,0.866104241,0.1109808993,0.3435986079
C,0,-0.5570608044,0.4726701363,0.2297867167
C,0,1.2176057256,-1.1878218306,0.9213190893
C,0,-1.5673114789,-0.2173884183,1.0975623767
C,0,-0.9281332696,1.8862977169,-0.12502655
H,0,1.6895587914,1.4689874097,-1.1114074729
H,0,2.8889927771,0.51211837,-0.2267281093
H,0,2.0665379217,1.8674102612,0.5692822582
H,0,0.7520317377,-1.931893108,0.2166146408
H,0,0.7588980546,-1.37381894,1.8985771058
H,0,2.2974314644,-1.3424749878,0.979326544
H,0,-1.4109181961,0.0715865562,2.1436724026
H,0,-1.486669076,-1.302010136,0.9951949657
H,0,-2.5809833822,0.0739169891,0.8054038431
H,0,-0.2488187935,2.332406772,-0.8550651998
H,0,-0.9238752671,2.508594148,0.7787699192
H,0,-1.9388845732,1.9038966926,-0.5455062051
O,0,-0.2303970465,-0.2712726627,-1.0462259151
O,0,-0.5937895824,-1.5789655228,-1.0830961432

1O2tme_INTtoPDT_UB1B95_6-31+Gdp_gasphaseIRC_INT.log
E(UB1B95) = -385.978553679

Zero-point correction= 0.171392 (Hartree/Particle)
Thermal correction to Energy= 0.181556
Thermal correction to Enthalpy= 0.182500
Thermal correction to Gibbs Free Energy= 0.137012
Sum of electronic and ZPE= -385.807162
Sum of electronic and thermal Energies= -385.796998
Sum of electronic and thermal Enthalpies= -385.796054
Sum of electronic and thermal Free Energies= -385.841542

	E	CV	S
	KCal/Mol	Cal/Mol-K	Cal/Mol-K
Total	113.928	37.199	95.738

C,0,1.9652442452,0.8720949048,-0.2432557814
C,0,0.8199820435,0.0208995974,0.2131741948
C,0,-0.5593475312,0.5477775578,0.3149699706
C,0,1.162498229,-1.2420850546,0.929766516
C,0,-1.5526971314,-0.1966912383,1.1440388919
C,0,-0.894950712,1.9687023677,-0.0225342215
H,0,1.6622126356,1.6561486722,-0.9334877578
H,0,2.7088691524,0.2465578751,-0.7396666636
H,0,2.4417102838,1.3372320863,0.6242570634
H,0,0.5702502781,-2.0383367524,0.4577937041
H,0,0.9067961516,-1.1896653917,1.9891582767
H,0,2.2229922766,-1.471906502,0.831968169
H,0,-1.2127492134,-0.3015574089,2.1757789432
H,0,-1.6631180543,-1.1914322204,0.6946198559
H,0,-2.5186652666,0.3075940762,1.1409121559
H,0,-0.2345986534,2.3938474818,-0.7749148911
H,0,-0.8329383727,2.5814827095,0.8810399011
H,0,-1.9191989677,2.0220608585,-0.3950466967
O,0,-0.1629522678,-0.2219520242,-0.9718765184
O,0,-0.6672101254,-1.5125275948,-1.1253561121

1O2tme_INTtoPDT_UB1B95_6-31+Gdp_gasphaseIRC_TS2.log
E(UB1B95) = -385.976335338

Zero-point correction= 0.170292 (Hartree/Particle)
Thermal correction to Energy= 0.179616
Thermal correction to Enthalpy= 0.180560
Thermal correction to Gibbs Free Energy= 0.137035
Sum of electronic and ZPE= -385.806043
Sum of electronic and thermal Energies= -385.796720
Sum of electronic and thermal Enthalpies= -385.795776
Sum of electronic and thermal Free Energies= -385.839300

	E	CV	S
--	---	----	---

	KCal/Mol	Cal/Mol-K	Cal/Mol-K
Total	112.710	34.850	91.604

C,0,1.9416802728,1.0560805115,-0.1042305545
 C,0,0.8822790483,0.1294367149,0.3878382608
 C,0,-0.5467490579,0.4625697962,0.2281609525
 C,0,1.2050082808,-1.1924130686,0.8804482571
 C,0,-1.5591261272,-0.2162989765,1.1082798252
 C,0,-0.9108264839,1.8801698613,-0.1309587809
 H,0,1.7223709153,1.4234772416,-1.108531669
 H,0,2.910419866,0.5581030158,-0.1270490324
 H,0,2.0234221807,1.9295674295,0.5524627485
 H,0,0.6800888414,-1.8575763209,0.1016356301
 H,0,0.7232706926,-1.4564058725,1.8232800298
 H,0,2.2725997671,-1.3990105734,0.915389674
 H,0,-1.453297801,0.1513849059,2.1313254293
 H,0,-1.4278992918,-1.2957978275,1.0879931416
 H,0,-2.5680131333,0.0071255565,0.760021787
 H,0,-0.2551009123,2.2905624371,-0.897076166
 H,0,-0.8489748257,2.5156391373,0.7558541375
 H,0,-1.9346841445,1.9112911528,-0.5052950489
 O,0,-0.2888979628,-0.2730149085,-1.0590848209
 O,0,-0.5717111248,-1.5936362125,-1.0389968007

1O2me_INTtoPDT_UCAM-B3LYP_6-31+Gdp_gasphaseIRC_INT.log
 E(UCAM-B3LYP) = -385.973545877

Zero-point correction= 0.172382 (Hartree/Particle)
 Thermal correction to Energy= 0.182417
 Thermal correction to Enthalpy= 0.183361
 Thermal correction to Gibbs Free Energy= 0.138163
 Sum of electronic and ZPE= -385.801164
 Sum of electronic and thermal Energies= -385.791129
 Sum of electronic and thermal Enthalpies= -385.790185
 Sum of electronic and thermal Free Energies= -385.835383

	E	CV	S
	KCal/Mol	Cal/Mol-K	Cal/Mol-K
Total	114.468	36.768	95.126

C,0,1.9703769613,0.8709414482,-0.242811764
 C,0,0.8175142508,0.0145783107,0.202738709
 C,0,-0.5639450071,0.5425069373,0.3059819456
 C,0,1.17878835,-1.2438815561,0.9339967641
 C,0,-1.5703697416,-0.1931360331,1.1396488339
 C,0,-0.9026538176,1.9689601379,-0.0279777377
 H,0,1.6701481647,1.6888110653,-0.8954528495
 H,0,2.6944294476,0.2520247185,-0.7785008494
 H,0,2.4705566137,1.2905163402,0.6363299307
 H,0,0.5731663979,-2.0536027213,0.5099356158

H,0,0.9703007129,-1.157549668,2.0032704867
 H,0,2.2361263367,-1.4786928005,0.8006661818
 H,0,-1.2203514419,-0.3206107601,2.1670212387
 H,0,-1.7172270152,-1.1781895156,0.6810040351
 H,0,-2.5221914834,0.3403478153,1.1570537862
 H,0,-0.2235108665,2.4124580864,-0.7539707096
 H,0,-0.8783138094,2.5704503815,0.8867479882
 H,0,-1.9164104045,2.0142062406,-0.4335934455
 O,0,-0.1558440905,-0.2212761793,-0.9693109531
 O,0,-0.6684605578,-1.5306182477,-1.1314382071

1O2tme_INTtoPDT_UCAM-B3LYP_6-31+Gdp_gasphaseIRC_TS2.log
 E(UCAM-B3LYP) = -385.968880652

Zero-point correction= 0.170904 (Hartree/Particle)
 Thermal correction to Energy= 0.180124
 Thermal correction to Enthalpy= 0.181068
 Thermal correction to Gibbs Free Energy= 0.137639
 Sum of electronic and ZPE= -385.797976
 Sum of electronic and thermal Energies= -385.788757
 Sum of electronic and thermal Enthalpies= -385.787813
 Sum of electronic and thermal Free Energies= -385.831241

	E	CV	S
	KCal/Mol	Cal/Mol-K	Cal/Mol-K
Total	113.029	34.422	91.403

C,0,1.949782416,1.052912884,-0.1036289865
 C,0,0.8832033892,0.1233501074,0.3821866737
 C,0,-0.5484832541,0.456812256,0.2209055482
 C,0,1.2161073543,-1.1957250887,0.8700079398
 C,0,-1.5718314479,-0.2066002033,1.1103674331
 C,0,-0.9148412452,1.8807627134,-0.1337000832
 H,0,1.7131161758,1.4727380615,-1.0831137241
 H,0,2.9077579729,0.5355757863,-0.1741538399
 H,0,2.0672440172,1.8904711222,0.5952843582
 H,0,0.68103091,-1.8482806264,0.0693553882
 H,0,0.7263208994,-1.4809379461,1.8030417584
 H,0,2.2856706952,-1.3988526821,0.9044857938
 H,0,-1.4887370467,0.2024843112,2.1216828854
 H,0,-1.4398494565,-1.2856131179,1.1361953664
 H,0,-2.5764150376,-0.0018218359,0.7343870391
 H,0,-0.258939418,2.3004814019,-0.8956581477
 H,0,-0.8616198861,2.5120107643,0.7586714365
 H,0,-1.9383075025,1.9082024364,-0.5137321232
 O,0,-0.2985482957,-0.2743179977,-1.0619675268
 O,0,-0.5500812396,-1.6175443464,-1.0241071894

1O2tme_INTtoPDT_UwB97XD_6-31+Gdp_gasphaseIRC_INT.log
 E(UwB97XD) = -386.047376360

Zero-point correction= 0.172165 (Hartree/Particle)
 Thermal correction to Energy= 0.182219
 Thermal correction to Enthalpy= 0.183163
 Thermal correction to Gibbs Free Energy= 0.137696
 Sum of electronic and ZPE= -385.875212
 Sum of electronic and thermal Energies= -385.865158
 Sum of electronic and thermal Enthalpies= -385.864214
 Sum of electronic and thermal Free Energies= -385.909680

	E	CV	S
	KCal/Mol	Cal/Mol-K	Cal/Mol-K
Total	114.344	36.792	95.693

C,0,1.9700324433,0.872335999,-0.242945879
 C,0,0.8168120751,0.0141580475,0.2019553555
 C,0,-0.5638643841,0.5420248924,0.3054461064
 C,0,1.1760711146,-1.2443938105,0.9350595049
 C,0,-1.5685555313,-0.195335372,1.1404398704
 C,0,-0.9013944099,1.9700436359,-0.0278244249
 H,0,1.6725521703,1.6805955928,-0.9100715622
 H,0,2.7041911942,0.2513972574,-0.7628231741
 H,0,2.4545991512,1.3061827852,0.6382932749
 H,0,0.5698862496,-2.0537862436,0.5067890654
 H,0,0.9608544864,-1.1576831613,2.0033720813
 H,0,2.2341589145,-1.4797713398,0.8064288683
 H,0,-1.2141241338,-0.3257542837,2.1663590033
 H,0,-1.7141756039,-1.1807519247,0.678096287
 H,0,-2.5212093738,0.3371358408,1.1614332377
 H,0,-0.2321037182,2.4091388285,-0.7667977396
 H,0,-0.8562615136,2.5714745564,0.8864318254
 H,0,-1.9216900391,2.0198403379,-0.4168448705
 O,0,-0.1583177974,-0.2264738388,-0.9763163688
 O,0,-0.665332294,-1.5221337993,-1.1351414613

1O2tme_INTtoPDT_UwB97XD_6-31+Gdp_gasphaseIRC_TS2.log
 E(UwB97XD) = -386.043849529

Zero-point correction= 0.171026 (Hartree/Particle)
 Thermal correction to Energy= 0.180115
 Thermal correction to Enthalpy= 0.181059
 Thermal correction to Gibbs Free Energy= 0.138100
 Sum of electronic and ZPE= -385.872824
 Sum of electronic and thermal Energies= -385.863735
 Sum of electronic and thermal Enthalpies= -385.862791
 Sum of electronic and thermal Free Energies= -385.905749

	E	CV	S
	KCal/Mol	Cal/Mol-K	Cal/Mol-K
Total	113.024	34.320	90.413

C,0,1.9450324383,1.060307516,-0.1000645294
 C,0,0.8836682876,0.120137856,0.3832027114
 C,0,-0.5489033938,0.453247184,0.220594393
 C,0,1.2153889272,-1.2056431744,0.8599155975
 C,0,-1.570091211,-0.2080836064,1.1165440032
 C,0,-0.9059843484,1.8823078496,-0.1289793356
 H,0,1.7620448103,1.378146822,-1.1303107382
 H,0,2.9281688332,0.5887950772,-0.0584806914
 H,0,1.9682361855,1.9620342206,0.5239284494
 H,0,0.6808941644,-1.8575281418,0.0605802116
 H,0,0.7267376217,-1.4927507664,1.79403549
 H,0,2.2849395293,-1.4109732364,0.8928437648
 H,0,-1.4555098101,0.1769819463,2.1344814566
 H,0,-1.4556155492,-1.2909610942,1.1148879806
 H,0,-2.5784621661,0.0230004507,0.7658283483
 H,0,-0.2468360282,2.2999603059,-0.8909814131
 H,0,-0.8427144599,2.5071341193,0.7677110873
 H,0,-1.9306445931,1.920648018,-0.5059786877
 O,0,-0.3102965792,-0.2750560782,-1.0660132952
 O,0,-0.5674726584,-1.6055972678,-1.0372348028

1O2me_INTtoPDT_UX3LYP_6-31+Gdp_gasphaseIRC_INT.log
 E(UX3LYP) = -385.991961142

Zero-point correction= 0.170028 (Hartree/Particle)
 Thermal correction to Energy= 0.180325
 Thermal correction to Enthalpy= 0.181270
 Thermal correction to Gibbs Free Energy= 0.135835
 Sum of electronic and ZPE= -385.821933
 Sum of electronic and thermal Energies= -385.811636
 Sum of electronic and thermal Enthalpies= -385.810692
 Sum of electronic and thermal Free Energies= -385.856126

	E	CV	S
	KCal/Mol	Cal/Mol-K	Cal/Mol-K
Total	113.156	37.679	95.624

C,0,1.9716723833,0.8785615491,-0.2432367504
 C,0,0.8233963263,0.0235723888,0.2256927057
 C,0,-0.5593377791,0.552149718,0.3291749702
 C,0,1.1841199216,-1.2449271443,0.9398273773
 C,0,-1.5742680411,-0.1905292875,1.1461911306
 C,0,-0.898444335,1.9757037244,-0.0284925634
 H,0,1.6670506952,1.6694382529,-0.9282487852
 H,0,2.711177274,0.2513282147,-0.7493292464
 H,0,2.4605201742,1.3401046659,0.6235743295
 H,0,0.6045305678,-2.0519661835,0.4649028046
 H,0,0.9267869061,-1.204332456,2.0020552906
 H,0,2.2505860891,-1.4590179957,0.8434623512

H,0,-1.2198436185,-0.3837031045,2.1626875426
 H,0,-1.7446675925,-1.1539835558,0.6407054742
 H,0,-2.5144542413,0.3623217008,1.1998347127
 H,0,-0.2381803617,2.3976232822,-0.7858286627
 H,0,-0.8393231976,2.6016342889,0.8704367965
 H,0,-1.9252825985,2.0236950581,-0.4022799001
 O,0,-0.1688227282,-0.2493576412,-0.9993067741
 O,0,-0.6750868441,-1.5500714752,-1.1204838034

1O2me_INTtoPDT_UX3LYP_6-31+Gdp_gasphaseIRC_TS2.log
 E(UX3LYP) = -385.991506372

Zero-point correction= 0.169548 (Hartree/Particle)
 Thermal correction to Energy= 0.179160
 Thermal correction to Enthalpy= 0.180104
 Thermal correction to Gibbs Free Energy= 0.135911
 Sum of electronic and ZPE= -385.821958
 Sum of electronic and thermal Energies= -385.812347
 Sum of electronic and thermal Enthalpies= -385.811402
 Sum of electronic and thermal Free Energies= -385.855596

	E	CV	S
	KCal/Mol	Cal/Mol-K	Cal/Mol-K
Total	112.425	35.518	93.012

C,0,1.9524932216,1.0331861327,-0.1358766925
 C,0,0.8587456713,0.1297066255,0.3480014364
 C,0,-0.5724109479,0.4875357603,0.2378789234
 C,0,1.2216529712,-1.156958205,0.9740246087
 C,0,-1.578554175,-0.2227630234,1.1104186497
 C,0,-0.9768356867,1.8884634245,-0.1651587602
 H,0,1.6384485579,1.6917379926,-0.9460119585
 H,0,2.8049794634,0.4420202651,-0.4817208295
 H,0,2.3037021525,1.6636452689,0.693334559
 H,0,0.7673280645,-1.9290775316,0.2985086066
 H,0,0.7728867621,-1.3050101442,1.9603237325
 H,0,2.3023889633,-1.2970386271,1.0333950004
 H,0,-1.3846965223,0.000206745,2.1647189165
 H,0,-1.5161565946,-1.2997754806,0.9421498365
 H,0,-2.5926770042,0.1035746209,0.8678214711
 H,0,-0.3213294495,2.3166201492,-0.9236727212
 H,0,-0.9659959323,2.5439965749,0.713416823
 H,0,-1.9944012558,1.8720913236,-0.5647430092
 O,0,-0.2135120447,-0.2972113073,-1.0450711308
 O,0,-0.5586322146,-1.6276395641,-1.064731462